






ARTICLE

Small-molecule modulators of INAVA cytosolic condensate and cell-cell junction assemblies

Denis Chang^{1,3*} , Phi Luong^{1,2,3*} , Qian Li^{1,4*}, Jamie LeBarron¹ , Michael Anderson^{1,2} , Lee Barrett⁵, and Wayne I. Lencer^{1,2,3} 

Epithelial cells lining mucosal surfaces distinctively express the inflammatory bowel disease risk gene INAVA. We previously found that INAVA has dual and competing functions: one at lateral membranes where it affects mucosal barrier function and the other in the cytosol where INAVA enhances IL-1 β signal transduction and protein ubiquitination and forms puncta. We now find that IL-1 β -induced INAVA puncta are biomolecular condensates that rapidly assemble and physiologically resolve. The condensates contain ubiquitin and the E3 ligase β TrCP2, and their formation correlates with amplified ubiquitination, suggesting function in regulation of cellular proteostasis. Accordingly, a small-molecule screen identified ROS inducers, proteasome inhibitors, and inhibitors of the protein folding chaperone HSP90 as potent agonists for INAVA condensate formation. Notably, inhibitors of the p38 α and mTOR pathways enhanced resolution of the condensates, and inhibitors of the Rho-ROCK pathway induced INAVA's competing function by recruiting INAVA to newly assembled intercellular junctions in cells where none existed before.

Introduction

The chronic inflammatory bowel diseases (IBDs) result from complex and still largely unexplained interactions among host, environmental, and genetic factors (Xavier and Podolsky, 2007). C1ORF106, recently renamed innate immune activator (INAVA; Yan et al., 2017), was identified as a risk gene for IBD by genome-wide association studies and targeted exome sequencing (Rivas et al., 2011). Human macrophages carrying the IBD risk allele rs7554511 have decreased levels of INAVA expression and show multiple defects in myeloid function (Yan et al., 2017). Transcripts for the protein are uniquely enriched in polarized simple epithelia, the primary cell type that forms the mucosal barrier (Nelms et al., 2016). Murine intestinal cells with the IBD risk SNP encoding INAVA Y333F have low expression of the INAVA protein, and mice lacking the protein entirely exhibit defects in intestinal barrier function (Manzanillo et al., 2018; Mohanan et al., 2018).

We recently proposed that INAVA acts to maintain epithelial homeostasis (Luong et al., 2018). In human intestinal epithelial cells, INAVA exhibits dual activities mechanistically linking epithelial barrier function and inflammatory signaling by interleukin 1 β (IL-1 β ; Luong et al., 2018). This is driven by INAVA's signature domain of unknown function 3338, which we renamed

cytohesin ubiquitin protein-inducing domain (CUPID). In Ca-co2BBe epithelial cells, the INAVA CUPID domain stably binds the GTP-exchange factor cytohesin-2 ARNO. At lateral membranes, the INAVA-ARNO complex affects cortical F-actin assembly to enhance cell-cell junctions and epithelial barrier function. In response to the inflammatory cytokine IL-1 β , INAVA relocates from lateral membranes to form cytosolic puncta and to amplify the activity of the E3 ubiquitin ligase TRAF6 and its inflammatory signaling. The two activities appear to be physically separated between lateral membranes and the cytosol, and possibly competing, as ARNO was found to diminish INAVA's effect on protein ubiquitination and IL-1 β signal transduction (Luong et al., 2018). How the cytosolic INAVA puncta contribute to either of these activities remains unknown.

In this study, we characterized the IL-1 β -induced cytosolic INAVA puncta. We found that they are biomolecular condensates: membraneless intracellular compartments formed by liquid-liquid phase separation. The results of high-content, image-based, small-molecule screens for puncta formation and inhibition implicate INAVA in processes that sense and regulate cellular proteostasis and, as we found before, in the assembly and maintenance of cell-cell junctions contributing to epithelial

¹Division of Gastroenterology and Nutrition, Department of Pediatrics, Boston Children's Hospital, Boston, MA; ²Harvard Digestive Disease Center, Boston, MA; ³Department of Pediatrics, Harvard Medical School, Boston, MA; ⁴Shanghai Children's Hospital, Shanghai Jiaotong University, Shanghai, China; ⁵F.M. Kirby Neurobiology Center, Translational Neuroscience Center, Boston Children's Hospital and Harvard Medical School, Boston, MA.

*D. Chang, P. Luong, and Q. Li contributed equally to this paper; Correspondence to Wayne I. Lencer: wayne.lencer@childrens.harvard.edu; Phi Luong: phi.luong@childrens.harvard.edu.

© 2021 Chang et al. This article is distributed under the terms of an Attribution-Noncommercial-Share Alike-No Mirror Sites license for the first six months after the publication date (see <http://www.rupress.org/terms/>). After six months it is available under a Creative Commons License (Attribution-Noncommercial-Share Alike 4.0 International license, as described at <https://creativecommons.org/licenses/by-nc-sa/4.0/>).

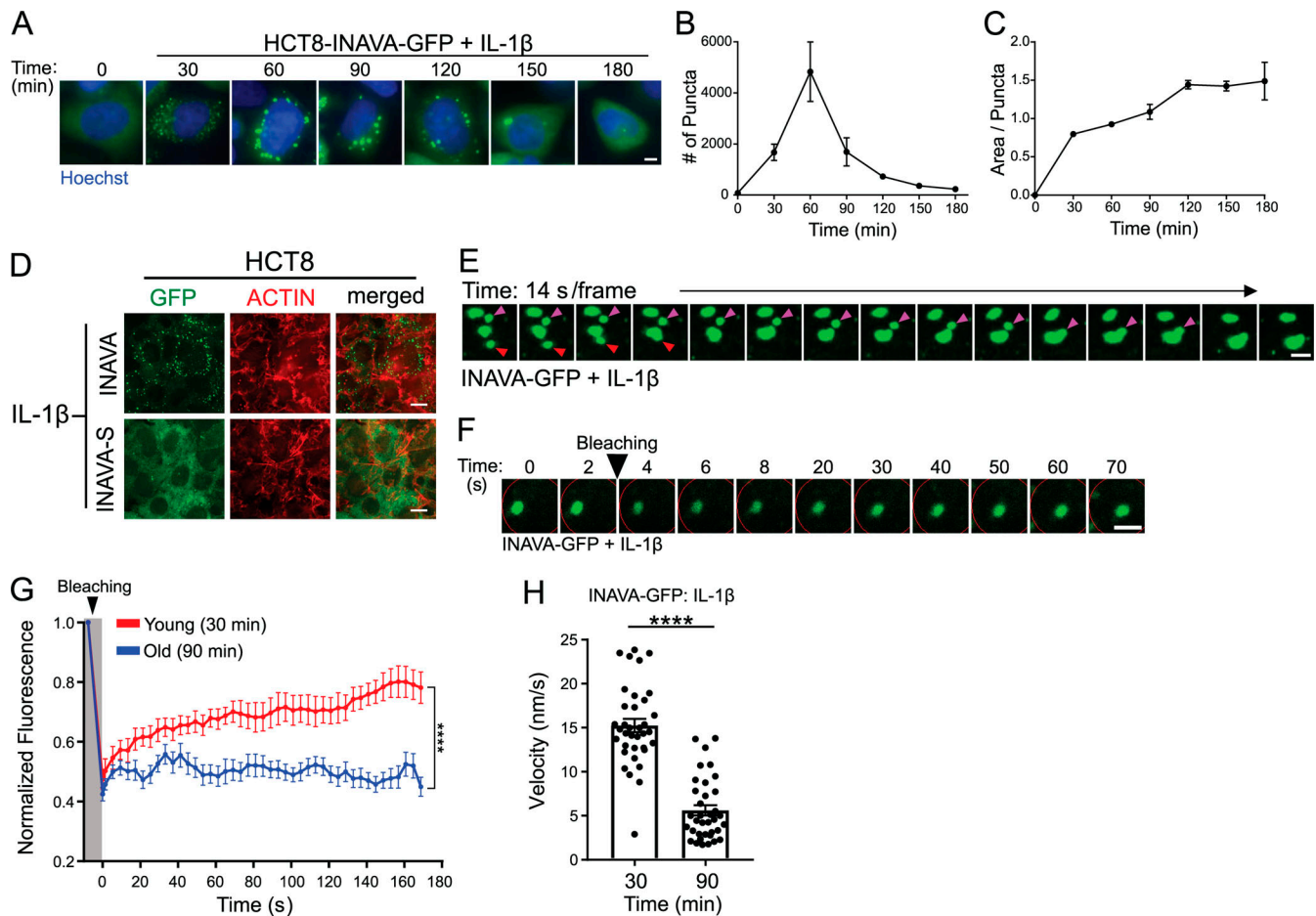


Figure 1. IL-1 β -induced INAVA puncta are biomolecular condensates. (A) Time course of condensate formation in HCT8-INAVA-GFP cells treated with IL-1 β . Scale bar = 5 μ m. (B) Quantification of puncta per 1,000 cells, mean \pm SD, $n = 2$. Images acquired at four positions/well. (C) As in B but analyzed by puncta area. (D) HCT8 cells expressing the long or short isoform of INAVA treated with IL-1 β for 90 min. Scale bar = 10 μ m. (E) IL-1 β -induced puncta fusion over time in HCT8 cells. Scale bar = 2 μ m. (F) FRAP of IL-1 β -induced puncta at 30 min. Scale bar = 2 μ m. (G) FRAP of “young” (30 min) and “old” (90 min) puncta, mean \pm SEM, $n = 10$. (H) Velocity tracking of puncta, mean \pm SEM, $n = 36$. ****, $P < 0.0001$.

integrity and barrier function. These key functions of INAVA are competing and dictated by the interchange of INAVA between membrane-bound and cytosolic biomolecular condensate assemblies.

Results

IL-1 β -induced INAVA puncta are biomolecular condensates

We began by studying the lifetime of IL-1 β -induced INAVA puncta in HCT8 epithelial cells stably expressing INAVA fused to GFP and the HA epitope (henceforth termed HCT8-INAVA-GFP cells; Fig. 1, A–C). As before (Luong et al., 2018), puncta formation was specific to the long isoform of INAVA (Fig. 1 D and Fig. S1 A), indicating specificity and suggesting physiological relevance. The human alternative short splicing isoform, lacking the N-terminal region (termed INAVA-S), did not form puncta (Fig. 1 D). In cells expressing the long isoform, however, we observed rapid formation of IL-1 β -dependent micrometer-scale puncta and their near-complete resolution over the course of 3 h. We noted that as the number of puncta diminished, the remaining puncta grew in size as if some puncta may have fused

together (Fig. 1, A and C). The observation suggested features of biomolecular condensates. Biomolecular condensates are micrometer-sized membraneless organelles that behave as phase boundary-separated liquids (Alberti et al., 2019; Lin et al., 2015). To test whether the INAVA-GFP puncta (henceforth termed INAVA puncta) possessed characteristics of liquid-liquid phase separation, we performed live cell imaging of HCT8-INAVA-GFP cells and observed fusion of puncta over time, suggesting liquid-like behavior (Fig. 1 E; and Videos 1 and 2). INAVA puncta did not colocalize with transferrin-positive endosomes or LAMP1-positive lysosomes (Fig. S1 B). In addition, FRAP studies also demonstrated the liquid behavior typifying molecular condensates (Alberti et al., 2019; Shin and Brangwynne, 2017). Following photobleaching, we found near-complete recovery of fluorescence within seconds, consistent with rapid diffusion of INAVA between puncta and the surrounding cytosol (Fig. 1 F and Video 3). Condensates are also described to undergo a process called maturation where their dynamic, highly mobile nature changes over time and they become more static and less fluid (Lin et al., 2015). Time course studies showed this result. Newly formed “young” INAVA puncta (≤ 30 min of IL-1 β treatment)

moved with greater mobility in the cytosol compared with “old” puncta imaged 60 min later. We also found that young puncta recovered more quickly and more completely following photo-bleaching, suggesting greater fluidity (Fig. 1, G and H). These features identify young INAVA puncta as biomolecular condensates.

A small-molecule approach to delineate the biology of INAVA condensates

Biomolecular condensates operate in key physiological cellular processes (Alberti, 2017; Alberti and Hyman, 2021; Banani et al., 2017; Lyon et al., 2020; Shin and Brangwynne, 2017). Our earlier studies implicated INAVA puncta in inflammatory signaling and protein ubiquitination (Luong et al., 2018). To understand how this may work and what factors induce or inhibit INAVA condensate formation, we developed a high-content, image-based, small-molecule screen for puncta formation and inhibition using HCT8-INAVA-GFP cells. HCT8 cells lack α -catenin and do not normally assemble intercellular junctions or tight epithelial monolayers (Vermeulen et al., 1997). As such, INAVA-GFP localizes diffusely in the cytosol, but it still robustly assembles into cytosolic puncta in response to IL-1 β (Luong et al., 2018). This clear signal resulting from converting a diffusely weak cytosolic fluorescence to discrete, intensely fluorescent puncta enabled a high-throughput, high-content imaging approach.

The screen we developed used curated libraries of small molecules with well-annotated functions and molecular targets (Fig. S1 C). Our approach was fully automated. Puncta were quantified using the MetaXpress High Content Image Acquisition and Analysis Software (Fig. S1 D). Z-factors for puncta formation were first calculated using several parameters (total number of puncta, puncta area, and puncta intensity). We used the most robust measure with the highest Z-factor for subsequent studies: the number of puncta per cell after 90 min of treatment. Using this parameter, a robust Z-factor of 0.588 was obtained (Fig. S1 E; Zhang et al., 1999). All images were also manually reviewed. Each compound was tested in duplicate, and >1,000 individual cells were imaged per condition and treatment.

We performed two screens: one to identify compounds that induced formation of INAVA puncta (Fig. 2 A, schematic) and another to identify compounds that inhibited puncta formation (Fig. 2 B, schematic). In the first screen (Fig. 2 A), HCT8-INAVA-GFP cells treated with IL-1 β were used as positive controls, and untreated cells were used as negative controls. In the second screen (Fig. 2 B), HCT8-INAVA-GFP cells were pretreated with each compound for 180 min before applying IL-1 β . Puncta formation was assessed after 90 min. In this screen, cells treated with only IL-1 β provided the negative controls (marking puncta formation), and cells completely untreated provided the positive controls (lack of puncta formation).

In total, we screened >6,000 unique compounds across a variety of well-annotated libraries available through the Harvard Institute of Chemistry and Cell Biology (ICCB) Longwood screening facility (Fig. S1 C). Compounds that resulted in cell death or intrinsic fluorescence were excluded from analysis. Z-scores for the induction of puncta formation (screen 1) or inhibition of puncta formation (screen 2) were calculated relative

to the negative control for each screen. Results are plotted by rank order of Z-score in Fig. 2, A and B. 422 and 726 negative controls independently assessed in screens 1 and 2, respectively, showed near-normal Gaussian distributions (plotted to the right of each figure). In the first screen, 41 small molecules with reproducible Z-scores >4.75 were considered for secondary validation (Fig. 2 A), and in the second screen, 40 small molecules with reproducible Z-scores <-2.35 were considered (Fig. 2 B).

Reactive oxygen species, heat shock protein 90, and proteasome inhibitors induce INAVA puncta

Of the 41 compounds selected for validation in the first screen, 29 (71%) were confirmed to be agonists for the formation of INAVA condensates as evidenced by dose-dependence studies (Table 1; Fig. 3, A and B; and Fig. S2, A-D). None of the validated agonists, including IL-1 β , induced visible condensates in control HCT8 cells overexpressing GFP alone (Fig. S2 E). The validated list includes three functionally related sets of compounds: proteasome inhibitors, compounds that induce reactive oxygen species (ROS), and inhibitors of the cytosolic chaperone heat shock protein 90 (HSP90). Each of these compounds caused the induction of INAVA condensates in the absence of any other stress stimuli, and all are related to processes underlying protein metabolism, implying that INAVA may sense and respond to changes in cell proteostasis.

Most notably, five HSP90 inhibitors induced INAVA puncta, and four of these exhibited half maximal effective concentrations (EC50s) in nM (Table 1; and Fig. 3, A and B). The most potent was ganetespib with EC50 of 15 nM. The HSP90 inhibitors, as evidenced by ganetespib and 17-N-allylamino-17-demethoxygeldanamycin (17AAG), appeared to act very rapidly, with newly formed “young” puncta (i.e., condensates) discerned just 5 min after application (Fig. 3, C and D). This is much faster in onset of action compared with the inflammatory cytokine IL-1 β , suggesting that HSP90 may regulate INAVA function more directly. Also, unlike the condensates induced by IL-1 β , continuous treatment with HSP90 inhibitors induced INAVA condensates that did not completely resolve over time (Fig. 3, D and E), and they took on larger and more irregular shapes (Fig. 3 E). Similar results were found for condensates induced by continuous treatment with the proteasome inhibitors MG132 and bortezomib and by hydrogen peroxide (H₂O₂), although these condensates displayed almost no evidence for resolution over time (Fig. 3, D and E). EC50s for the proteasome inhibitors MG132 and bortezomib were 2.2 and 0.33 μ M, respectively (Fig. S2 B). Both compounds have previously been shown to induce the formation of condensates known as stress granules (Fournier et al., 2010; Hofweber et al., 2018; Mateju et al., 2017). Similarly, though with less potency, three compounds that generate ROS, and a thiol oxidizing reagent, also induced INAVA condensates (Table 1 and Fig. S2 D). This result was confirmed using H₂O₂ (Fig. 3, D and E).

The older puncta imaged 90 or 120 min after IL-1 β , H₂O₂, or ganetespib treatment colocalized with vimentin, although unexpected staining of the nucleus was also found. The result, however, suggested maturation of condensates to aggresomes (Kopito, 2000), as further evidenced by the lack of vimentin

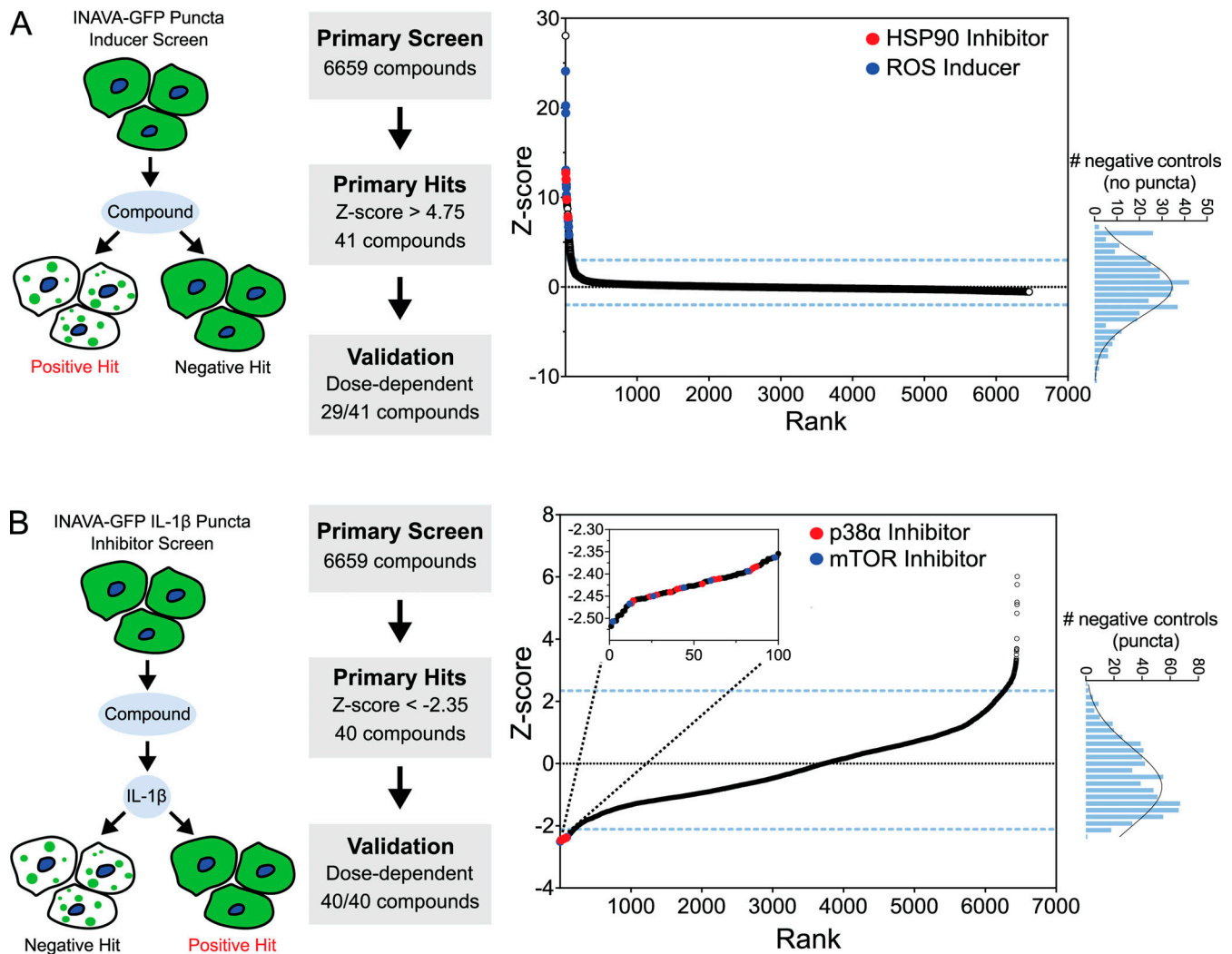


Figure 2. **A small-molecule approach to delineate the biology of INAVA condensates.** (A) Schematic (left panel) and results (middle panel) of screen for inducers of INAVA-GFP puncta. Ranked Z-scores are shown on the right panel; several highly ranked HSP90 inhibitors (red) or ROS inducers (blue) are indicated. Frequencies of distribution of negative controls are displayed to the right of graph. (B) Schematic (left panel) and results (middle panel) of screen for compounds that block IL-1 β -induced puncta. Ranked Z-scores are shown on the right panel; a high proportion of top hits were MAPK p38 α (red) and mTOR (blue) inhibitors. Frequencies of distribution of negative controls are displayed to the right of graph.

colocalization in the younger puncta (Fig. 3 F and Fig. S2 F). Review of the BioGRID protein interaction database (<https://thebiogrid.org>) suggests that INAVA associates with the dynein-dynactin complex (and thus microtubules), also consistent with maturation of INAVA condensates to aggresomes (Fig. S2 G). None of the mature INAVA puncta induced by IL-1 β , H₂O₂, ganetespib, or MG132, however, stained for the presence of amyloid (Fig. S2, H and I), and the mature puncta induced by IL-1 β or H₂O₂ did not colocalize with the stress granule proteins G3BP1 or EDC4 (also a P-body protein; Fig. 3 G and Fig. S2 J) or with HDAC6 (Fig. S2 K). Thus, in several cases, maturation of INAVA condensates appeared to take on some, but not all features that typify aggresomes (Kopito, 2000).

In the case of cells treated with H₂O₂, ganetespib, or MG132, we reasoned that the lack of puncta resolution over time could reflect the nonphysiological nature of continuous drug treatment, structural differences in the condensates formed, or both.

As such, HCT8-INAVA-GFP cells were exposed to short (30-min) pulses of each compound, washed free of drug, and then observed for an additional 4 h. Under these conditions, puncta were uniformly induced by short pulses of each compound tested. Puncta fully resolved after compound removal in cells treated with IL-1 β , H₂O₂, or ganetespib, implicating down-regulation and physiological relevance (Fig. S2 L). The puncta induced by MG132, however, did not visually resolve. The mature puncta induced by continuous HSP90 inhibitor, MG132, and H₂O₂ treatments were, in all cases, associated with reduced INAVA expression as assessed by immunoblot against the HA epitope, consistent with resolution by puncta degradation even as they coalesced visually (Fig. 3 F; and Fig. S2, M and N). In contrast, INAVA expression remained stable when puncta were induced by the inflammatory cytokine IL-1 β (Fig. S2 M), suggesting, in this case, resolution by puncta disassembly. Thus overall, depending on the stimulus, the mature

Table 1. Validated small compounds that induce INAVA puncta

Z-score	Compound	Mechanism	EC50 (μM)
24.1	BAPTA-AM	Ca ²⁺ chelator	33.2
20.2	Thimerosal	Thiol oxidizing reagent	14.7
19.4	Furoxan	ROS inducer	94.3
12.7	Geldanamycin	HSP90 inhibitor	1.2
12.6	2043 D17	Undetermined	8.8
12.6	MG132	Proteasome inhibitor	2.2
12.0	Bortezomib	Proteasome inhibitor	0.33
12.0	17-Allylamino-geldanamycin	HSP90 inhibitor	0.07
12.0	Ganetespib	HSP90 inhibitor	0.02
11.4	Fascaplysin	Cdk inhibitor	3.4
10.0	Parthenolide	Sesquiterpene lactone	49.8
9.8	Beta-lapachone	Topoisomerase inhibitor	30.4
9.7	NVP-AUY922	HSP90 inhibitor	0.07
8.8	PKI/Akt/Flt dual pathway inhibitor		0.83
8.8	KX01	Tubulin inhibitor	0.72
8.7	AV-412	EGFR/HER2 inhibitor	50.8
8.1	Herbimycin A	Tyrosine kinase inhibitor	4.4
7.8	Radicicol	HSP90 inhibitor	0.12
7.7	Albendazole	Tubulin inhibitor	18.6
7.5	Oxibendazole	Tubulin inhibitor	25.5
7.0	NS-1619	K-channel activator	202.8
6.7	LY-83583	ROS inducer	6.8
6.6	Cytochalasin D	Actin inhibitor	10.8
5.9	Latrunculin B	Actin inhibitor	69.0
5.8	Auranofin	Mitochondrial thioredoxin reductase inhibitor	7.5
5.8	3407 J11	Undetermined	34.1
5.1	5z-7-oxozeanol	TAK1 inhibitor	22.1
4.9	Gramicidin	Antibacterial	9.1
4.9	Z-leu3-VS	Proteasome inhibitor	42.8

EGFR, epidermal growth factor receptor; HER, human epidermal growth factor receptor.

INAVA condensates varied in their gross morphologies, in their time of onset after agonist exposure, and when and if they resolved, suggesting different structural compositions and mechanisms underlying their assembly and resolution, although other explanations may be possible.

INAVA condensates as a mediator of cellular proteostasis

We recently observed that the INAVA CUPID domain acted to amplify TRAF6-dependent protein ubiquitination *in vitro* (Luong et al., 2018), and given the results of our small-molecule screen, we reasoned that the INAVA condensates may function in regulation of cellular proteostasis by perhaps assembling the machinery for protein ubiquitination. As a first test of this idea, we used the FK2 ubiquitin antibody to immunostain for protein-conjugated ubiquitin (Fujimuro et al., 1994). We uniformly

observed colocalization of INAVA-GFP with FK2-ubiquitin within the condensates (Fig. 4 A and Fig. S3 A) and with the promiscuous E3 ubiquitin ligase FBXW11 (βTrCP2; Fig. 4 B and Fig. S3 B). βTrCP2 was recently implicated as an INAVA-interacting protein (Mohanani et al., 2018). When overexpressed on its own, however, myc-βTrCP2 did not form cytosolic puncta (Fig. S3 C). This result implicates dependence on INAVA as a structural or recruiting element for condensate assembly with βTrCP2 or perhaps that INAVA provides a substrate for ubiquitination by βTrCP2, thus enabling puncta assembly on ubiquitin chain scaffolds (Sha et al., 2009), or both.

To more directly test the idea that INAVA condensates may function in the regulation of cellular proteostasis, we measured total protein ubiquitination and its correlation with puncta formation. We studied HEK293T cells expressing HA-tagged

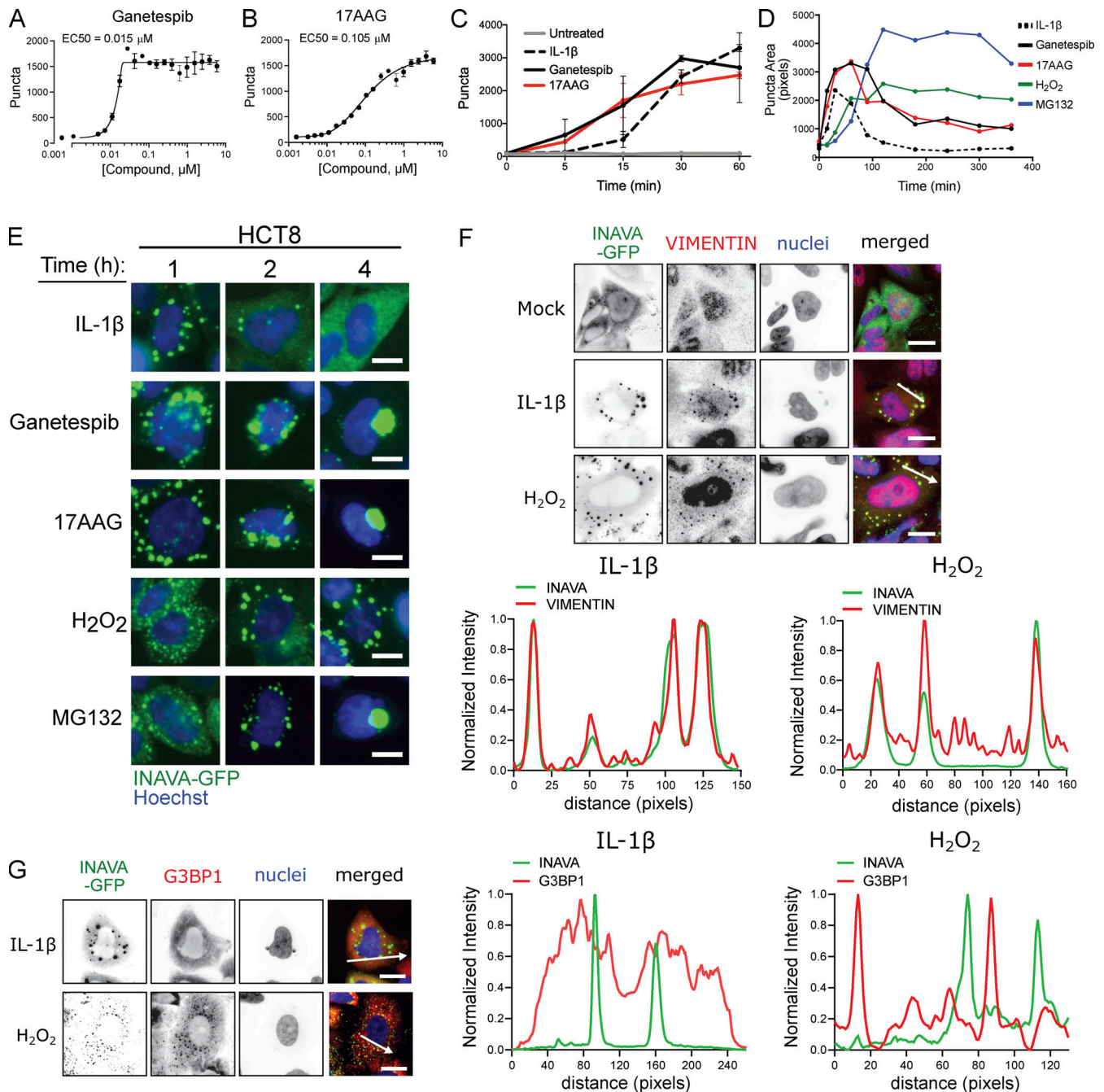


Figure 3. **ROS and HSP90 and proteasome inhibitors induce INAVA puncta.** (A and B) Dose response for HSP90 inhibitors (A) ganetespiib and (B) 17AAG, mean \pm SEM, $n = 3$. (C) Time course of puncta formation by IL-1 β (10 ng/ml), ganetespiib (1 μ M) and 17AAG (10 μ M), mean \pm SD, $n = 2$. (D) Time course of puncta formation and resolution after treatment with agonists noted above, $n = 2$. (E) Time course images from D. Scale bar = 10 μ m. (F and G) Confocal images of HCT8-INAVA-GFP cells stained for (F) vimentin or (G) G3BP1 following treatment with IL-1 β or H₂O₂ for 90 min. Hoechst (nuclei). Line scans (arrows) display relative fluorescence intensity of INAVA and (F) vimentin or (G) G3BP1. Scale bar = 20 μ m.

ubiquitin and the long or short isoforms of GFP-INAVA (lacking the HA tag) or a mutant form of GFP-INAVA (termed C/A) that contains the substitution of a conserved cysteine for alanine at a site in the CUPID domain surrounded by hydrophobic residues. We hypothesized that this region may form an active enzymatic site underlying INAVA function. We found that H₂O₂ broadly induced protein ubiquitination but only in HEK293T cells expressing the long isoform of INAVA, the isoform that assembles

into cytosolic puncta (Fig. 4 C). Cells expressing the short isoform, which do not form puncta, or cells expressing INAVA with the putative inactivating C/A substitution, showed no evidence for enhanced protein ubiquitination. These results correlate INAVA puncta formation with protein ubiquitination induced by cell stress (ROS). While INAVA may itself be a substrate for the ubiquitination reactions, the broad band of ubiquitinated proteins detected in cells after H₂O₂ treatment, spanning a wide range of

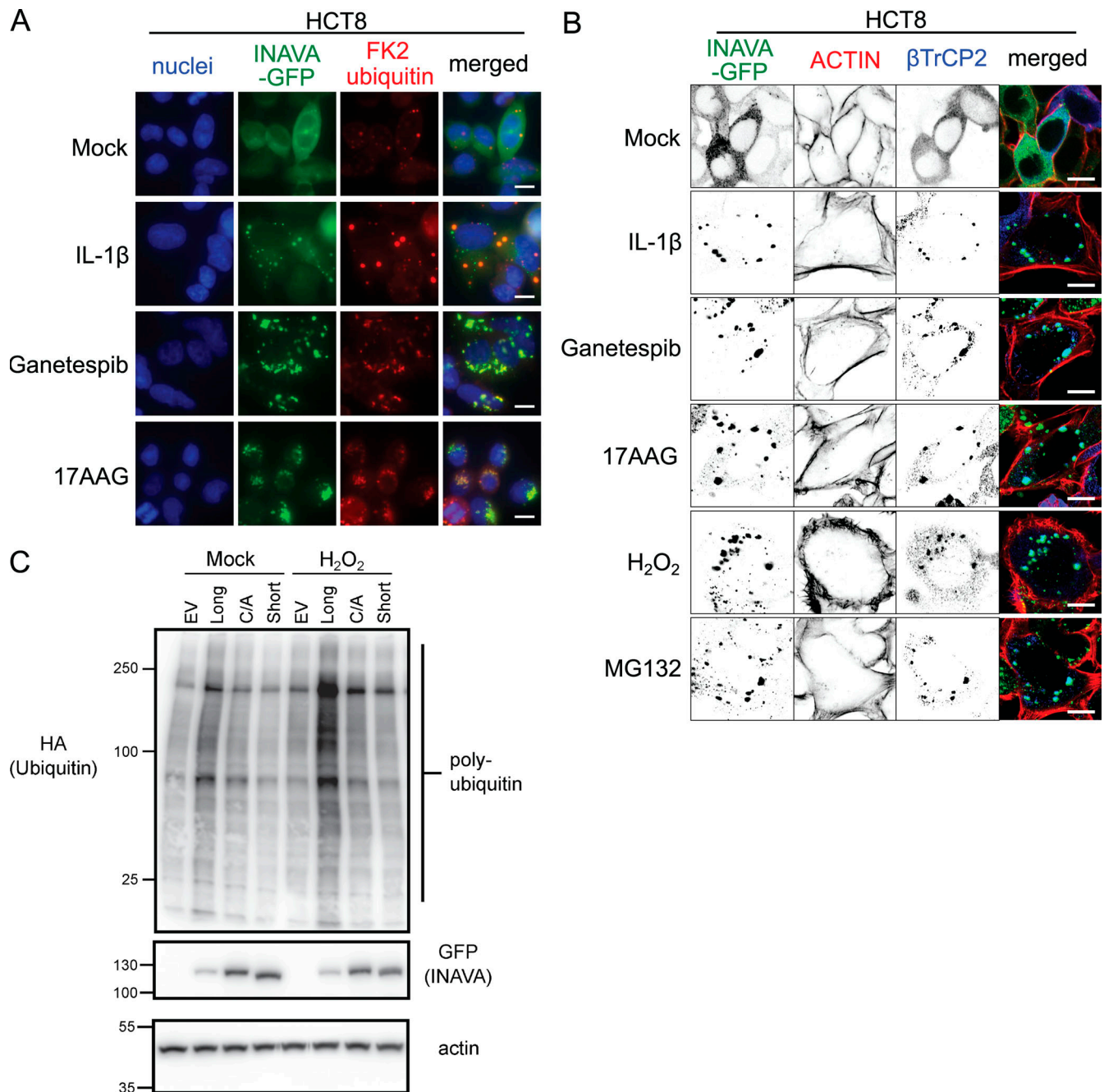


Figure 4. **INAVA condensates as a mediator of cellular proteostasis.** (A) HCT8-INAVA-GFP cells were treated with IL-1 β (10 ng/ml) for 1 h and ganetespib (1 μ M) and 17AAG (10 μ M) for 1.5 h. Cells were fixed and stained with conjugated ubiquitin antibody FK2. Scale bar = 10 μ m. (B) HCT8-INAVA-GFP cells expressing doxycycline-inducible myc- β TrCP2 were treated with doxycycline (1 μ g/ml) overnight followed by the condensate inducers as in A or H₂O₂ (1 mM) for 90 min. Cells were fixed and stained with α -myc for β TrCP2. Scale bar = 10 μ m. (C) HEK293T cells were transfected with HA-ubiquitin with stably expressed empty vector (EV), GFP-INAVA long or short isoform, and a CUPID domain mutant (C141A). Cells were treated with or without H₂O₂ (1 mM) for 90 min. Whole-cell lysates were collected and analyzed by immunoblot for HA (ubiquitin), GFP (INAVA), and actin. The unit of measure for the Western blots is kilodaltons.

apparent molecular weights, suggests that INAVA promotes ubiquitination of many proteins other than itself.

Inhibitors of the MAPK p38 α and mammalian target of rapamycin pathway induce the resolution of INAVA condensates

Of the 40 compounds selected for validation in the second screen, all of them (100%) were confirmed as condensate

antagonists by dose-response studies (Table 2; and Fig. S4, A–D). The validated list includes three functionally related sets of compounds. The top-ranked “hit” was the inhibitor of protein translation cycloheximide, followed closely by emetine. Both have been shown before to antagonize other molecular condensates, thus implicating RNA, the ribosome, and nascent protein translation in condensate formation or maintenance (Mokas et al., 2009; Thomas et al., 2009). Nearly half of the

Table 2. Validated small compounds that block IL-1 β -induced INAVA condensates

Z-score	Compound	Mechanism	IC50 (μ M)
-2.52	Cycloheximide	Protein synthesis inhibitor	0.16
-2.51	INK-128	mTOR inhibitor	0.04
-2.51	K-252a	PKA/C/G inhibitor	2.63
-2.51	PDGF receptor tyrosine kinase inhibitor III		6.71
-2.50	Anisomycin	Protein synthesis inhibitor	0.06
-2.49	Lycorine	Protein synthesis inhibitor	3.86
-2.48	5z-7-oxozeaenol	TAK1 inhibitor	0.09
-2.47	NVP-BHG712	EPHB4 inhibitor	1.3
-2.47	DCC-2036	Bcr-Abl kinase/TIE/VEGF receptor inhibitor	2.0
-2.47	GDC-0980	mTOR inhibitor	2.2
-2.47	p38 MAPK inhibitor VIII	p38 MAPK inhibitor	0.06
-2.46	PD 169316	p38 MAPK inhibitor	0.31
-2.46	BX795	TBK1/PDK1 inhibitor	2.3
-2.45	PI-3Ka inhibitor IV	mTOR inhibitor	3.95
-2.45	RWJ-67657	p38 MAPK inhibitor	0.07
-2.45	OTSSP167	MELK inhibitor	0.05
-2.45	GNE-493	mTOR inhibitor	1.06
-2.45	LY2228820	p38 MAPK inhibitor	0.05
-2.44	Emetine	Protein synthesis inhibitor	0.03
-2.44	IKK-2 inhibitor XI		26.9
-2.44	AV951	VEGF receptor inhibitor	166.3
-2.44	SB203580	p38 MAPK inhibitor	2.4
-2.44	KW-2449	FLT3 inhibitor	63.7
-2.44	AMG-47a	LCK inhibitor	0.23
-2.43	VX702	p38 MAPK inhibitor	0.22
-2.43	SB202190	p38 MAPK inhibitor	0.69
-2.43	BEZ235	mTOR inhibitor	0.21
-2.43	AMG-Tie2-1	Tie-2 inhibitor	4.07
-2.43	PH-797804	p38 MAPK inhibitor	0.05
-2.43	IKK-2 inhibitor VI		5.2
-2.42	IKK inhibitor VII		0.28
-2.42	GTPL6019	PDGF receptor tyrosine kinase inhibitor	12.5
-2.42	NG25	Multiple kinase inhibitor	2.4
-2.42	KU0063794	mTOR inhibitor	6.4
-2.41	SB239063	p38 MAPK inhibitor	38.3
-2.40	IKK-2 inhibitor IV		4.1
-2.39	PI-103	mTOR inhibitor	291.7
-2.39	GW856553X	p38 MAPK inhibitor	0.06
-2.39	SB242235	p38 MAPK inhibitor	2.2
-2.38	SB220025	p38 MAPK inhibitor	11.5

other validated compounds fell into two functionally related groups: 12 (30%) are known inhibitors of the MAPK p38 α , and 7 (18%) are known inhibitors of the mammalian target of rapamycin (mTOR) complex (Table 2; and Fig. 5, A and B). The

results associated the two kinases with regulation of INAVA condensate formation or their resolution.

To address these ideas, we used the mTOR inhibitor INK128 (half maximal inhibitory concentration [IC50], 0.04 μ M) and

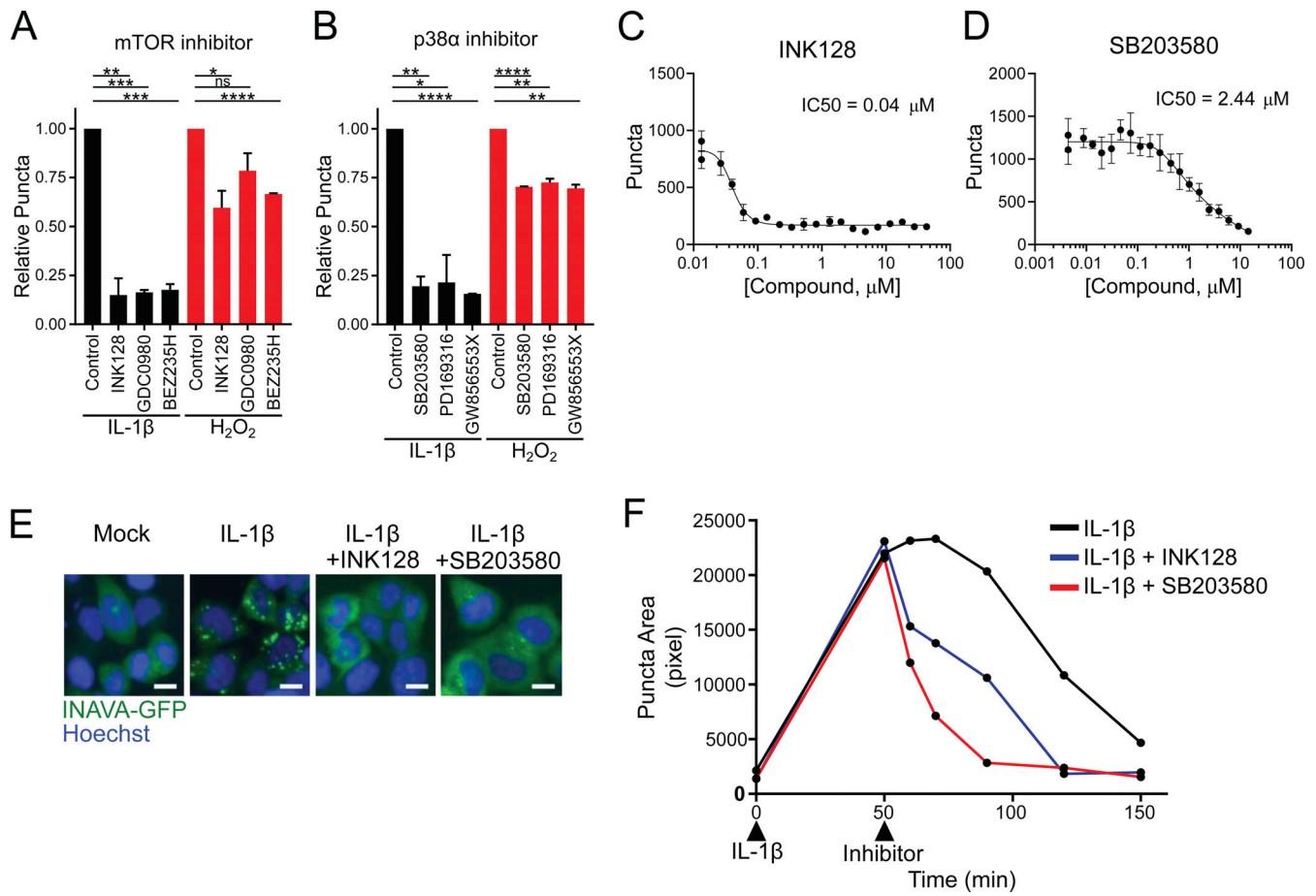


Figure 5. Inhibitors of the MAPK p38 α and mTOR pathway induce the resolution of INAVA condensates. (A and B) In HCT8-INAVA-GFP cells, IL-1 β - and H₂O₂-induced INAVA-GFP condensates are blocked by mTOR inhibitors (A) and p38 α inhibitors (B). Graphs display results from high-content imaging, mean \pm SD, $n = 2$. (C and D) Dose–response curves for (C) mTOR inhibitor INK128 or (D) p38 α inhibitor SB203580, mean \pm SEM, $n = 3$. (E) High-content images from dose–response studies. HCT8-INAVA-GFP cells were pretreated with INK128 (43 μ M) or SB203580 (14 μ M) for 30 min followed by IL-1 β (10 ng/ml) for 90 min. Scale bar = 5 μ m. (F) Cells were treated with IL-1 β (10 ng/ml) for 50 min followed by INK128 (10 μ M) or SB203580 (10 μ M) then fixed and stained with Hoechst (nuclei) at indicated time points, $n = 2$ independent experiments. *, $P < 0.05$; **, $P < 0.01$; ***, $P < 0.001$; ****, $P < 0.0001$.

the p38 α inhibitor SB203580 (IC₅₀, 2.4 μ M; Fig. 5, C and D). Pretreatment of HCT8-INAVA-GFP cells with either compound INK128 or SB203580 resulted in near-complete block of IL-1 β -induced INAVA condensates (Fig. 5, A–E). To test whether these inhibitors acted by enhancing the resolution of condensates, we first treated HCT8-INAVA-GFP cells with IL-1 β for 50 min to allow peak condensate formation and then applied the inhibitors. Normally, INAVA condensates induced by IL-1 β assemble and then resolve within 3 h (Fig. 1 B and Fig. 5 F, black line). We found that both compounds caused a more rapid decrease in INAVA condensates, as assessed by condensate area (Fig. 5 F, red and blue lines). Notably, we did not detect degradation of INAVA. Both results suggest puncta resolution by disassembly (Fig. S4 E). We do note, however, that 1,6-hexanediol, a known inhibitor of some biomolecular condensates (Wheeler et al., 2019) failed to inhibit the INAVA puncta induced by IL-1 β (Fig. S4, F and G).

With identification of the INK128 or SB203580 inhibitors, we could now test whether condensate formation is required for the amplification of TRAF6-dependent IL-1 β inflammatory signaling

by INAVA that we previously observed (Luong et al., 2018). We prepared HCT8-INAVA-GFP cells transiently expressing the nuclear factor- κ B (NF- κ B)-dependent luciferase reporter transgene (as described Luong et al., 2018). The reporter cell line was then treated with IL-1 β alone or following pretreatment with INK128 or SB203580. Neither compound affected the amplification of IL-1 β -induced NF- κ B signaling caused by INAVA overexpression (Fig. S4, H and I). We also found that TRAF6 did not colocalize with the INAVA condensates (Fig. S4 J). Thus, the ability of INAVA to amplify IL-1 β -induced TRAF6-dependent NF- κ B signaling appears to occur independently of (or before) INAVA condensate formation, suggesting a separate function (or location) for INAVA in inflammatory signal transduction, an event also dependent on ubiquitination.

Blockade of INAVA and FUS, FMR1, and FXR1 condensates

Continuous exposure to ROS (H₂O₂) induced INAVA condensates that appeared to follow a process of maturation described for other biomolecular condensates (Lin et al., 2015). This was evidenced by the loss of liquid-like behavior (Fig. S4 K

and Video 4) and loss of cytosolic mobility (Fig. S4 L). As some mature condensates are implicated in human disease (Alberti and Dormann, 2019), we tested whether the mTOR and p38 α inhibitors might resolve the “older” H₂O₂-induced INAVA puncta. We found that mTOR and p38 α inhibitors only partially resolved these mature puncta (Fig. 5, A and B). As such, we performed a semi-orthogonal screen to identify more effective antagonists for H₂O₂-induced puncta (Fig. S4 M). The Z-factor for this screen was 0.747 (Fig. S1 E). As anticipated, the p38 α and mTOR inhibitors were not among the top hits (Table S1). However, the protein translation inhibitors cycloheximide, emetine, and other compounds, including the maternal embryonic leucine zipper kinase (MELK) inhibitor OTSSP167, emerged again as antagonists of INAVA puncta, in this case, effective against condensates with mature biophysical and biochemical features (Table 2 and Table S1).

As both the mTOR and MELK inhibitors can affect protein synthesis (Dennis et al., 2012; Wang et al., 2016), we next tested whether they blocked INAVA condensate formation by decreasing INAVA expression and thus its effective cytosolic concentration (Alberti, 2017; Banani et al., 2017; Boeynaems et al., 2018). We found that all three inhibitors—INK128 (mTOR), OTSSP167 (MELK), and cycloheximide—with or without IL-1 β , had no effect on INAVA-GFP expression as measured by Western blot (Fig. S4, E and N). Thus, the level of INAVA expression cannot explain the mechanism(s) of puncta formation or resolution.

We next tested these compounds on condensates formed by proteins implicated in human disease (Alberti and Dormann, 2019; Bureau et al., 2017; Elbaum-Garfinkle, 2019; Takata et al., 2017) as modeled in HeLa cells containing FUS-GFP (as transgene) or FMR1 and FXR1 (endogenously expressed). Condensates containing these molecules were induced using sodium arsenate or the proteasome inhibitor MG132. We found that both INK128 and OTSSP167, but not SB203580, antagonized FUS-GFP, FMR1, and FXR1 stress-induced condensate formation (Fig. 6, A–E). If applied after their formation, however, neither INK128 nor OTSSP167 enhanced puncta resolution (Fig. S5 A). Thus, INK128 and OTSSP167 appear to act by preventing formation of FUS-GFP, FMR1, and FXR1 condensates rather than by enhancing their disassembly or degradation.

RhoA kinase inhibitors rescue epithelial morphology in HCT8 cells

We noticed by visual inspection that two inhibitors of RhoA kinase (ROCK) rapidly recruited INAVA to newly formed HCT8 cell–cell contact sites that contained the tight junction adaptor protein ZO-1 (Fig. 7, A–C). Although these inhibitors have previously been shown to recruit junction proteins to existing cell–cell contacts of epithelial monolayers (Sahai and Marshall, 2002), this was a notable and unanticipated finding as HCT8 cells do not normally form tight intercellular junctions at all (Vermeulen et al., 1997). Similar results were obtained with blebbistatin, which inhibits myosin II, a downstream effector of the Rho–ROCK pathway. These findings suggested that blockade of ROCK signaling might restore epithelial junctions and barrier function. To test this idea, we grew HCT8-INAVA-GFP and parent (WT) HCT8 cells in Matrigel. We assessed their

formation of spheroid cyst-like structures that typifies an early step in epithelial barrier morphogenesis (Ivanov et al., 2008). In both cases, spheroid cysts were observed, indicating the development of cell polarity and cell–cell junctions, although the cysts formed by WT HCT8 cells had dysmorphic, fingerlike projections (Fig. 7 D, first and second row, and Fig. 7 E). When treated with the ROCK inhibitor Y27632, the WT HCT8 cysts developed drastically perturbed cell morphologies (Fig. 7 D, third row), consistent with previous reports (Ivanov et al., 2008). Strikingly, overexpression of INAVA completely abrogated this effect (Fig. 7 D, fourth row). Structurally, the cysts formed by cells treated with the ROCK inhibitors were more well organized than those formed in the absence of ROCK inhibition (Fig. 7 D, compare fourth row with second row). The results of these studies are quantified in Fig. 7 E and imply that INAVA functionally intersects with the Rho–ROCK pathway to effect junction assembly and epithelial polarization.

INAVA’s functions at lateral membranes and in cytosolic condensates are competing reactions

According to our model for the duality of INAVA functions (Luong et al., 2018), we tested the prediction that the newly identified agonists for condensate formation should also induce the displacement of INAVA from lateral membranes. Here, we used the human intestinal Caco2BBE cell line. Unlike HCT8 cells, Caco2BBE cells form cell–cell junctions that lead to INAVA localization on the membrane (Luong et al., 2018). These studies showed the predicted results: All newly identified agonists induced the release of INAVA from lateral membranes of Caco2BBE cells and the formation of large cytosolic puncta (Fig. S5, B and C).

We previously observed competing functions for INAVA in IL-1 β inflammatory signal transduction and at intercellular junctions dictated by its binding to ARNO via the CUPID domain (Luong et al., 2018), an intrinsically disordered region typical of proteins forming biological condensates (Fig. S1 A; Han et al., 2012). Discovery of the ROCK inhibitors as inducers of lateral membrane INAVA cell junction assemblies allowed us to retest this model. We reasoned that if competing functions for INAVA are driven by the interchange between lateral membranes and cytosolic condensates, the ROCK inhibitors should act as antagonists of condensate assembly. Upon review of our screen results, we found that HCT8-INAVA-GFP cells treated with the ROCK inhibitors formed INAVA condensates in lower numbers and that this phenotype was dose dependent (Fig. 7 F and Fig. S5 D). On the other hand, our results also showed that the myosin II inhibitor blebbistatin had no effect. Myosin II is a downstream effector of the Rho–ROCK pathway, but it is not the only effector (Riento and Ridley, 2003).

To test whether the two functions of INAVA are split between cytosolic and membrane locations as suggested, we used HCT8-INAVA-GFP cells overexpressing the doxycycline-inducible and catalytically inactive ARNO mutant E156K tagged with the myc-epitope (termed ARNO-E156K). Here, we found the predicted results: Overexpression of ARNO-E156K phenocopied the ROCK inhibitors and relocalized INAVA-GFP to newly formed cell–cell contact sites of HCT8 cells (Fig. 7 G). Furthermore, when these cells were treated with IL-1 β , far fewer cytosolic INAVA

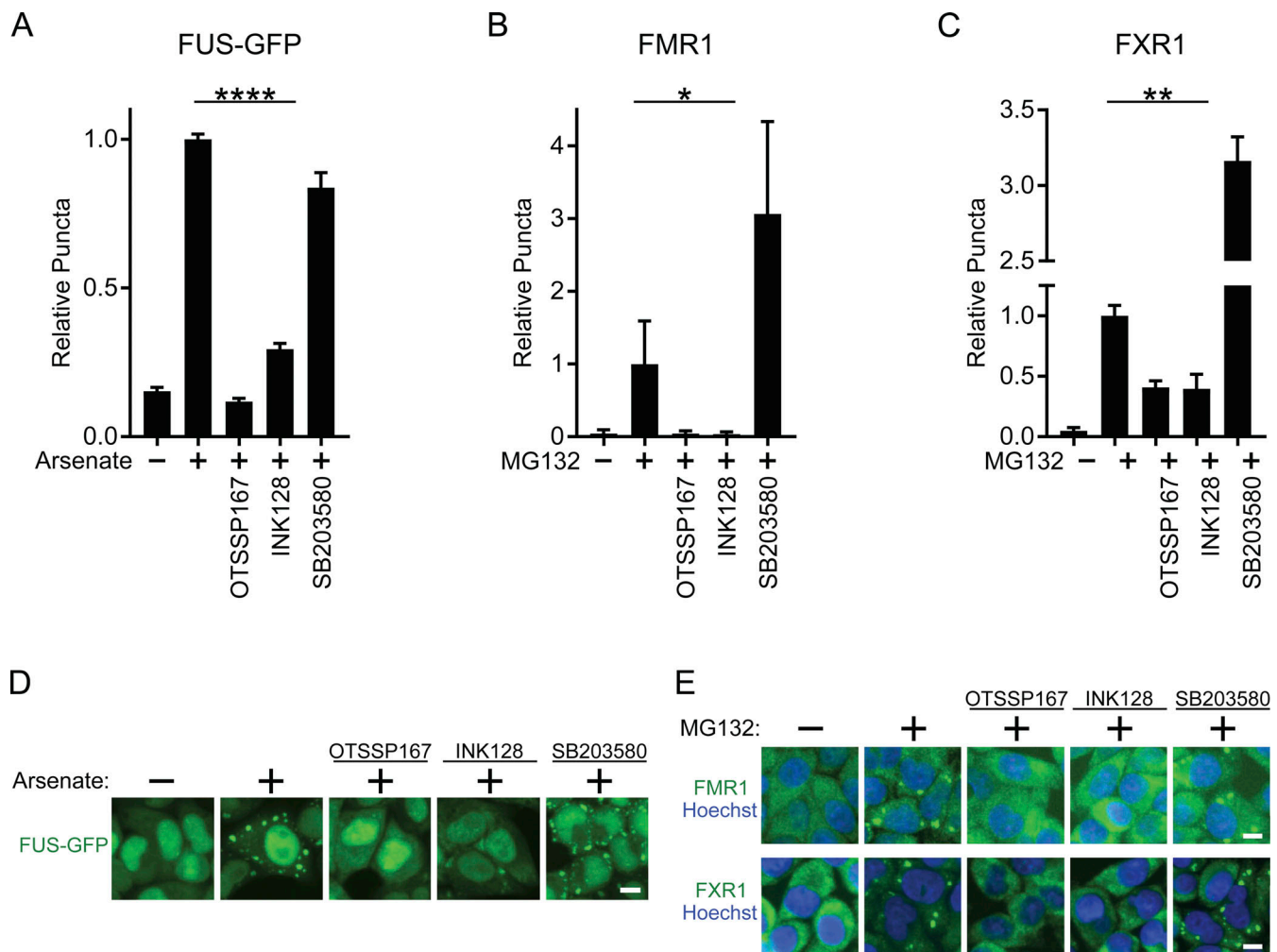


Figure 6. **Blockade of INAVA and FUS, FMR1, and FXR1 condensates.** (A) HeLa cells stably expressing FUS-GFP were pretreated with OTSSP167 (5 μ M), INK128 (10 μ M), or SB203580 (10 μ M) for 30 min followed by sodium arsenate (1 mM) for 90 min. Images were acquired at six positions/well at 20 \times magnification, mean \pm SD, $n = 6$. Reproduced in three independent studies. (B and C) As in A but with WT HeLa cells treated with MG132 (10 μ M) for 5 h. Cells were fixed and stained with (B) α -FMR1 or (C) α -FXR1. (D) FUS-GFP images from A. (E) Images of FMR1 and FXR1 from B and C. Scale bars = 10 μ m. *, $P < 0.05$; **, $P < 0.01$; ***, $P < 0.0001$.

condensates were formed (Fig. 7 H). Thus, the two functions of INAVA in regulating intercellular junctions and cellular proteostasis appear to be competing reactions. They are regulated by ARNO and dictated by the exchange of INAVA between molecular assemblies located in cytosolic condensates and those at lateral membranes.

Discussion

A small-molecule screen allowed us to assign the different functions of the IBD risk gene INAVA as competing processes dictated in part by intracellular location. One process occurs in cytosolic biomolecular condensates where upon cell stress, INAVA assembles with the promiscuous E3 ligase β TrCP2, conjugated ubiquitin, and likely other yet-to-be-identified factors to compartmentalize and regulate, we hypothesize, protein ubiquitination. This is perhaps best evidenced by our studies of newly ubiquitinated proteins in response to H₂O₂ using cells expressing the short, long, or mutant INAVA isoforms (Fig. 4 C).

The idea that INAVA condensates act to regulate protein ubiquitination is further suggested by our previous studies on INAVA's signature CUPID domain (Luong et al., 2018) and earlier evidence that INAVA and the E3 ligase β TrCP2 physically associate (Fig. S2 G; Mohanan et al., 2018). The other process occurs at cell-cell contact sites of the plasma membrane when INAVA binds the cytohesin ARNO and where it affects cell-cell junctions and mucosal barrier function (Luong et al., 2018).

The cytosolic condensates, however, do not appear to be required for INAVA's effect on IL-1 β -induced signal transduction, although early, nonvisible forms of condensates may be involved, as suggested by the circumstantial evidence that enhanced IL-1 β -induced TRAF6 signaling and puncta formation require the long isoform of INAVA. The short INAVA-S isoform, which cannot form cytosolic puncta, is inactive for both functions (Figs. 1 D and 4 C). How the N-terminal region of INAVA enables condensate assembly, however, remains unknown. The region is predicted to be unstructured and amenable for condensate assembly (Fig. S1 A; Banani et al., 2017; Lyon et al., 2020),

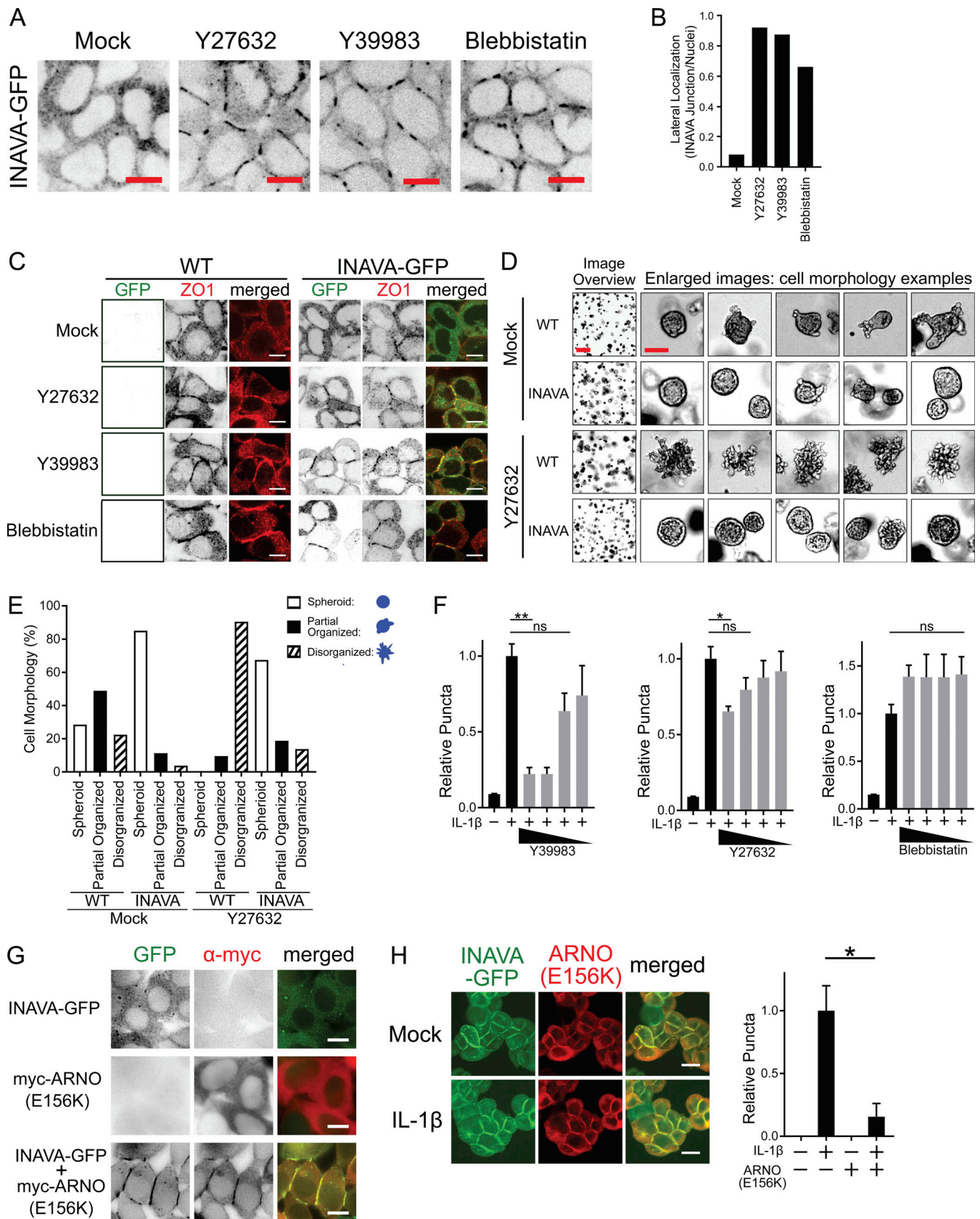


Figure 7. **ROCK inhibitors rescue epithelial morphology in HCT8 cells.** (A) Confocal images of HCT8-INAVA-GFP cells treated with ROCK inhibitors Y27632 (10 μM), Y39983 (10 μM), or myosin II inhibitor blebbistatin (50 μM) for 1 h. Scale bar = 10 μm. (B) Quantification of INAVA-GFP localized to lateral membranes, n = 120–150 cells/condition. (C) Confocal images of HCT8 WT and HCT8-INAVA-GFP cells treated as in A and stained with tight junction marker ZO-1. Scale bar =

10 μm . **(D)** Brightfield images of HCT8 WT and HCT8-INAVA-GFP cysts grown in Matrigel \pm Y27632 (10 μM). Overview scale bar = 500 μm . Enlarged image scale bar = 100 μm . **(E)** Relative distribution of HCT8 cyst morphology from D, $n = 80\text{--}98$ cysts/condition. **(F)** Dose response of ROCK inhibitor Y39983, Y27632, or blebbistatin (left to right, 33 μM , 6.7 μM , 1.3 μM , 0.3 μM) in blocking IL-1 β -induced condensates, mean \pm SEM, $n = 2$. **(G)** HCT8-INAVA-GFP cells with doxycycline-inducible GEF mutant myc-ARNO-(E156K). Cells were treated overnight with doxycycline (1 $\mu\text{g}/\text{ml}$), fixed, stained, and imaged at four positions/well at 40 \times magnification, $n = 2$. Scale bar = 10 μm . **(H)** Confocal images (left) and quantification (right) of puncta inhibition as in G but treated with IL-1 β (10 ng/ml) for 60 min. Scale bar = 20 μm , mean \pm SEM, $n = 2$. *, $P < 0.05$; **, $P < 0.01$.

and the CUPID and C-terminal domains also score as unstructured regions. Still, it is possible that a third site of function for INAVA exists for amplification of IL-1 β -dependent inflammatory responses: one that occurs in the cytosol before condensate formation and competes with INAVA-ARNO binding on lateral membranes. This is further evidenced by our observations that TRAF6 fails to colocalize with detectable INAVA condensates induced by IL-1 β and that downregulation of condensates by the p38 α and mTOR inhibitors did not significantly affect NF- κ B signaling. Thus, not all INAVA-enhanced protein ubiquitination reactions (in particular those involved in inflammatory signaling) may occur within condensate structures, although it remains possible that INAVA-TRAF6 signaling condensates may assemble differently and be too small for detection by our methods as discussed above.

The screen also revealed that INAVA likely responds to changes in the cellular proteome, notably by the rapid formation of condensates. This was evidenced following treatment with any of the five small-molecule inhibitors of the heat shock chaperone HSP90 and by the equally robust, though slower responses to H₂O₂, the small-molecule inducers of oxidative stress (ROS), and the inhibitors of the proteasome, all of which affect protein metabolism. Biomolecular condensates are membraneless organelles that concentrate the components required to propagate reactions underlying key subcellular functions (Alberti, 2017; Alberti and Hyman, 2021; Banani et al., 2017; Lyon et al., 2020; Shin and Brangwynne, 2017). Examples include the nucleolus, the P-body (Brangwynne et al., 2009), stress granules (Protter and Parker, 2016), the LAT system of actin assembly in T cells (Su et al., 2016), and cGAS in innate immunity (Du and Chen, 2018). Several condensates are known to assemble in response to cell stress (Alberti and Hyman, 2021; Banani et al., 2017). In the case of INAVA, we propose that the condensates may compartmentalize and regulate protein ubiquitination to selectively alter cellular proteostasis in response to cell stress or inflammation. Our results suggest two potential ways by which this may occur: (1) by concentrating the ubiquitination machinery and its substrates to enhance and specify protein ubiquitination or (2) by the opposite, restricting ubiquitin-mediated processes by sequestering key factors into condensates, making them inaccessible. The physiological significance of INAVA condensates will more definitively be elucidated through further identification of its components (Banani et al., 2016).

Proteotoxic stress induces INAVA condensates

We also newly identified small-molecule inhibitors of HSP90 as agonists for INAVA condensate formation. Previous studies have reported that other condensates can be induced by inhibition of the proteasome (Hofweber et al., 2018; Mateju et al., 2017) or by

induction of oxidative stress (Kato et al., 2019), also implicating condensate formation in response to altered cellular proteostasis. HSP90 functions as a molecular chaperone, rescuing the conformations of proteins misfolded in response to environmental or cell intrinsic stress, and it stabilizes the fold of normally metastable proteins (Taipale et al., 2012). Given the rapidity of inhibitor action on condensate formation, it is possible, though not conclusively shown, that INAVA may be a direct client of HSP90, as further evidenced by loss of INAVA expression after prolonged exposure to the HSP90 inhibitor ganetespib. Of note, we found that HSP90 inhibitors rapidly induced INAVA condensates distinct in shape, size, and half-life from those induced by the inflammatory cytokine IL-1 β . Similar differences in condensate morphology and half-life were found for INAVA condensates induced by ROS and the proteasome inhibitors. We propose that this reflects different compositions of the INAVA condensates, with specificity in structure and function dictated by the different agonists, as seen in stress granules (Protter and Parker, 2016).

Small-molecule inhibitors of biomolecular condensates

Inhibitors of mTOR and p38 α were identified as antagonists of IL-1 β -induced INAVA condensates. We found that both classes of inhibitors may function by amplifying the disassembly of the condensates and, thus, their resolution, but this remains to be experimentally confirmed and the mechanism(s) explained. mTOR is a serine/threonine-specific protein kinase that belongs to the family of phosphatidylinositol-3 kinases that operate fundamentally to regulate cell growth, survival, and cellular metabolism in response to the environment and internal cell stress (Saxton and Sabatini, 2017; Zhao and Goldberg, 2016). The MAPK p38 α is also a serine/threonine kinase. It is expressed in all cell types and operates widely in different cellular processes, including inflammatory signaling (Broom et al., 2009; Coulthard et al., 2009). Posttranslational phosphorylation of INAVA by these kinases may explain their mechanism of action in puncta resolution, but this has not yet been formally tested. Alternatively, inhibition of mTOR has been shown to alter the cellular proteome by the induction of autophagy (Saxton and Sabatini, 2017) and by amplifying protein ubiquitination (Zhao et al., 2015), and p38 α inhibitors alter the proteome by direct activation of the proteasome (Leestemaker et al., 2017). Interestingly, there have been reports of autophagic cargo (Danieli and Martens, 2018; Sun et al., 2018) and the proteasome itself (Yasuda et al., 2020) colocalized within phase-separated organelles (i.e., condensates). But here, degradative mechanisms of action likely do not explain resolution of the IL-1 β -induced INAVA condensates, as evidenced by the stability of INAVA expression during puncta resolution. In the case of INAVA

condensates induced by H₂O₂, many of the p38 α and mTOR inhibitors were only partially effective in inducing puncta resolution. These condensates have features that typify mature condensates containing proteins implicated in human neurodegenerative disease, namely FUS, FXR1, and FMR1. Here, we note that our screen identified compounds that inhibited the assembly of these “mature” condensates as modeled in HeLa cells, including new compounds operating in the mTOR, MELK, and other pathways (see Table 2 and Table S1), possibly with relevance to treatment of human disease.

INAVA at cell–cell junctions and its opposition to condensate formation

An unanticipated and striking finding was the discovery that several ROCK inhibitors rapidly relocated INAVA from the cytosol of HCT8 cells to the lateral membrane where cell–cell junctions were newly assembled and contained the tight junction scaffolding protein ZO-1. These results were notable given INAVA’s ability to relocate ARNO from cytosolic pools to lateral membranes of Caco2 monolayers, resulting in enhanced barrier function (Luong et al., 2018). A similar phenotype showing enhanced epithelial structure and development of barrier monolayers (epithelial cysts) was reproduced for the ROCK inhibitors using HCT8 cells grown in 3D culture. In this case, the effect was specific for cells expressing INAVA, as the dysmorphic cellular phenotype induced by ROCK inhibition was prevented. These results suggested to us that INAVA acts along with the Rho–ROCK pathway to affect epithelial morphogenesis, monolayer (cyst) formation, and epithelial barrier function.

Previous studies, however, have reported conflicting effects of ROCK inhibitors on epithelial barrier function. In cell culture, inhibition of ROCK caused increased paracellular epithelial permeability (Riento and Ridley, 2003), implying reduced tight junction structure and function, whereas in vivo, the ROCK inhibitors caused decreased mucosal permeability (Grothaus et al., 2018; Zou et al., 2018). The exact mechanisms for how ROCK inhibition induced the observed cell junction phenotypes and intersected with the INAVA–ARNO complex at lateral membranes remain to be determined.

Finally, we note that the functions of INAVA at the lateral membrane appear to be in opposition with its stress-induced activity of compartmentalizing and likely specifying ubiquitination reactions within cytosolic condensates. This is best evidenced by our current studies using cells overexpressing the enzymatically inactive mutant of ARNO and by our previous biochemical studies showing that ARNO blocks the enhancement of protein ubiquitination by binding INAVA’s CUPID domain (Luong et al., 2018). Overall, we hypothesize that INAVA may act as a sensor and effector of cellular proteostasis, with its sensing activity localized to lateral (plasma) membranes and its effector activity localized to cytosolic condensates containing the machinery for targeted protein ubiquitination. A proposed model for INAVA’s location-dependent function is depicted in Fig. 8. We consider it likely that the way INAVA may sense disruption of cellular proteostasis will involve concordant alterations in its mechanisms of assembly and function on the lateral membrane.

Materials and methods

Plasmids

INAVA-HA-GFP, which contains an HA and GFP tag (referred to as INAVA-GFP) and FUS-GFP, were cloned into pLVX-Efla-AcGFP-N1 (Clontech Laboratories). INAVA WT and mutant C141A long isoforms and INAVA-S (short isoform) were cloned into pLVX-Efla-AcGFP-C1 (Clontech Laboratories) to generate GFP-INAVA, GFP-INAVA (C141A), and GFP-INAVA-S to generate INAVA variants absent of HA tag. Doxycycline-inducible GEF mutant myc-ARNO-(E156K), myc-TRAF6, and myc- β TrCP2 were cloned into pCW57.1 (Harvard Plasmid Repository).

Antibodies and chemicals

Antibodies anti-myc (2276S), HDAC6 (7558S), FXR1 (12295T), and FMR1 (4317S) were purchased from Cell Signaling Technology; anti-ZO-1 (339100) and anti-G3BP1 (PA5-29455) from Thermo Fisher Scientific; and anti-vimentin (sc-6260) from Santa Cruz Biotechnology. Anti-EDC4 (SAB4200114) was purchased from Sigma. AMYLO-GLO (TR-300-AG) was purchased from VWR International. Anti-FK2 ubiquitin (BMLPW8810100) was purchased from Enzo Life Sciences, and anti-LAMP1 (H4A3) was purchased from Developmental Studies Hybridoma Bank. Phenol Red-free LDEV-free Matrigel (CB356239), Hoechst (H1399), DRAQ5 (62251), secondary Alexa Fluor antibodies, transferrin-Alexa Fluor 647 (T23366), bortezomib (5043140001), I7AAG (I1039), ganetespib (19432), and Y27632 (125410) were purchased from Thermo Fisher Scientific. INK128 (1224844385), SB203580 (152121476), and OTSSP167(1431698100) were purchased from Cayman Chemical. Blebbistatin (sc203532) was purchased from Santa Cruz Biotechnology. H₂O₂ (H1009), MG132 (474790), and sodium arsenate (A6756) were purchased from Sigma. IL-1 β (200-10B) was purchased from PeproTech. Phalloidin-TRITC was purchased from American Peptide.

Cell culture

HEK293T, HCT8, HeLa, and Caco2BBE cells were grown on DMEM 10% FBS with penicillin/streptomycin. HEK293T, HCT8, and Caco2BBE were authenticated using short tandem repeat analysis by American Type Culture Collection and tested negative for mycoplasma contamination. Stably expressed doxycycline-inducible myc-ARNO-(E156K) and HA-tagged HCT8-INAVA-GFP and Caco2BBE-INAVA-GFP cells were generated by lentivirus transduction. For ubiquitination experiments, HEK293T cells stably expressing empty vector; GFP-INAVA long, short; and cysteine 141 mutant were generated by lentivirus transduction and used for ubiquitination assays.

High-throughput small-molecule treatment

HCT8 cells overexpressing INAVA-GFP (HCT8-INAVA-GFP) were grown in media (DMEM, 10% FBS, 5% penicillin/streptomycin) and plated at 6,250 cells/well on 384-well plates (781090; Greiner Bio-One) using the Multidrop Combi Reagent Dispenser (Thermo Fisher Scientific). Cells were incubated overnight at 37°C before pin transfer.

Small-molecule libraries and individual cherry-picked compounds were obtained from ICCB-Longwood (<https://iccb.med.harvard.edu>). All compounds were screened in duplicate. For the

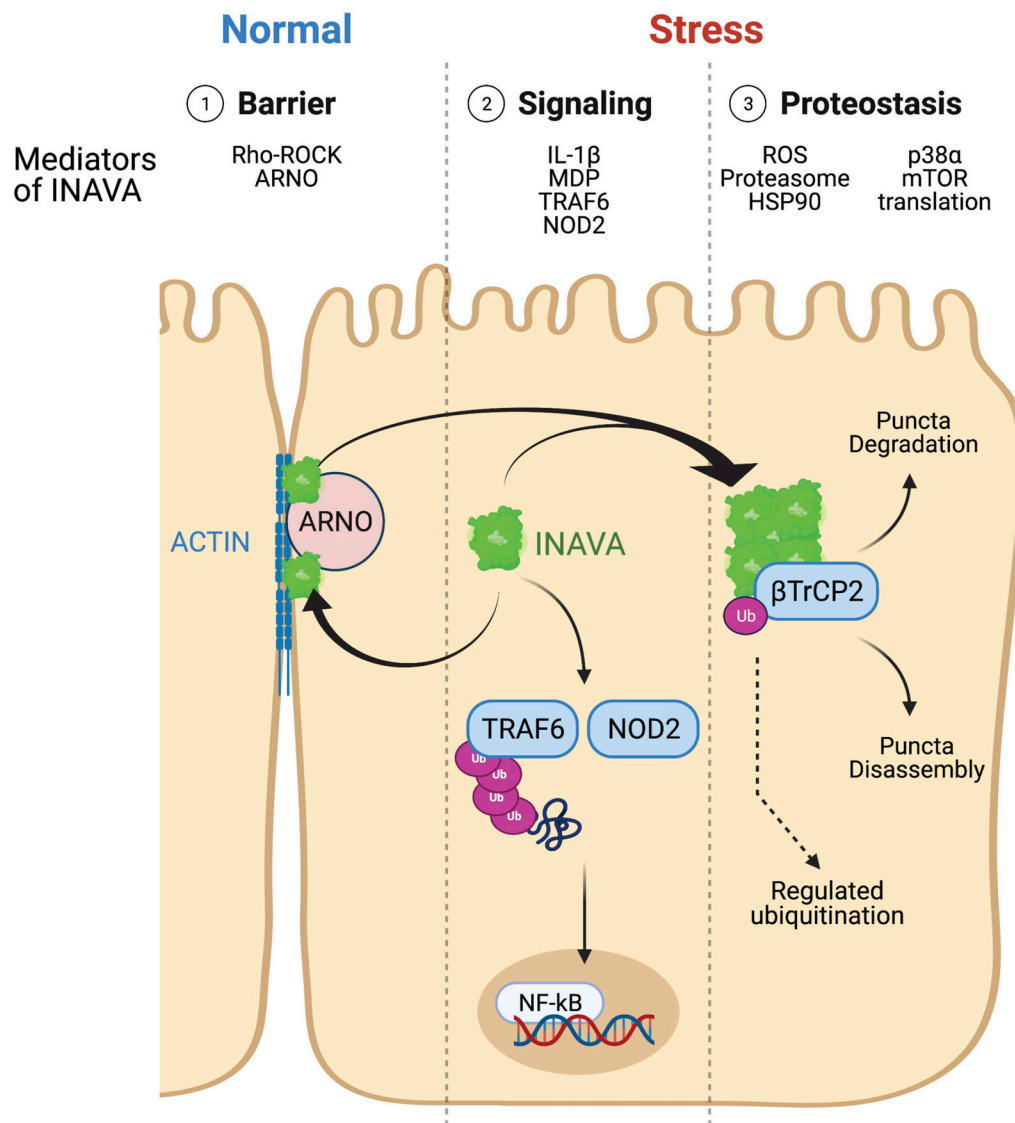


Figure 8. **Model of INAVA biology.** ARNO and inhibitors of the Rho-ROCK pathway mediate INAVA localization at cellular junctions. In the cytosol, INAVA promotes IL-1 β -TRAF6 inflammatory stress signaling and the muramyl dipeptide (MDP)-NOD2 pathway. Proteotoxic stress (ROS, inhibitors of HSP90 and the proteasome) induce cytosolic INAVA condensates containing the E3 ligase β TrCP2 and conjugated ubiquitin. Inhibitors of p38 α , mTOR, and translation induce the resolution of stress-induced INAVA condensates. Ub, ubiquitin.

condensate formation screen, compounds were pin transferred to HCT8-INAVA-GFP cells and incubated for 90 min at 37°C before fixing for imaging. For the condensate inhibition screen, HCT8-INAVA-GFP cells were pretreated with each compound for 180 min before applying IL-1 β (10 ng/ml) or H₂O₂ (1 mM) to induce condensate formation. Cells were incubated for 90 min at 37°C before fixing for imaging. The Mantis Liquid Handler (Formulatrix) was used to add IL-1 β or H₂O₂. Cells were fixed with 4% PFA (15713S; Electron Microscopy Sciences), and nuclei were stained with Hoechst (1:5,000).

High-content fluorescent imaging

The ImageXpress Micro Confocal High Content Imaging System (Molecular Devices) was used for automated imaging and analysis. High-content images were acquired at four positions/well at 20 \times magnification. Small-molecule screening images

were taken from at least four fields of view per well at 20 \times magnification. An image at 20 \times magnification is 2,048 pixels per x-y axis, where 1 pixel = 0.3423 μ m. Images were manually reviewed and reimaged if out of focus. Automatic quantification of INAVA-GFP puncta was performed using Granularity Analysis in MetaXpress High Content Image Acquisition and Analysis Software (Molecular Devices). Puncta per cell were calculated by dividing the total number of puncta in all four images per well by the total number of nuclei per well (puncta / nuclei). Z-scores based on puncta per cell were calculated using the formula $Z = (x - \mu) / \sigma$, where x represents the sample and μ and σ represent the mean and SD, respectively, for the total negative controls used across all plates for each screen.

Dose-dependent studies were performed to validate the results of each primary screen, selecting the top compounds based on Z-score. The same method was used as above to plate, treat,

fix, and image cells. The HPD300 Digital Dispenser (Tecan) was used to test 14 different concentrations for each compound in triplicate.

ImageXpress high-content imaging was used in HeLa cells stably expressing FUS-GFP and WT HeLa cells. FUS-GFP cells plated in 96-well plates (655090; Greiner Bio-One) were pre-treated with compounds where indicated for 1 h before treatment with 1 mM sodium arsenate for 90 min. Cells were fixed and stained with Hoechst (1:5,000). WT HeLa cells were pre-treated with compounds as indicated followed by treatment with MG132 (10 μ M) for 5 h. Cells were fixed and permeabilized as above. Cells were stained with anti-FXR1 (1:150) and anti-FMR1 (1:150) for endogenous staining. High-content images were taken as above using 20 \times magnification but at six fields of view per well. Puncta analysis was performed as described above. Time courses for condensate inducers (HSP90 inhibitor, proteasome inhibitor, H₂O₂, and IL-1 β) in HCT8-INAVA-GFP cells were fixed at indicated time points, imaged, and analyzed by high-content imaging as described above. To test whether pre-formed FUS-GFP puncta induced by arsenate can be resolved, HeLa FUS-GFP cells were treated with arsenate for 90 min, followed by INK128 (10 μ M) or OTSSP167 (5 μ M). Cells were fixed at indicated time points using 4% PFA, imaged, and analyzed as above.

For ubiquitin localization, HCT8-INAVA-GFP cells were plated on 96-well plates and imaged and analyzed as described above for ImageXpress Micro confocal high-content imaging or 24-well plates (P240N; Cellvis) and imaged with the Zeiss 880 confocal microscope. Cells were treated with IL-1 β (10 ng/ml), ganetespib (100 nM), or 17AAG (500 nM) and incubated at 37°C for 120 min. Cells were fixed with 4% PFA, washed with 0.2% saponin, and blocked with 5% goat serum for 1 h. Cells were incubated with anti-FK2 ubiquitin (1:500) overnight at 4°C. The following day, cells were washed with 0.2% saponin and incubated with secondary Alexa Fluor antibody (1:500) and Hoechst (1:5,000) for 1 h and rinsed with PBS before imaging.

FRAP

FRAP experiments were performed on the Zeiss 880 laser scanning confocal microscope with Fast Airyscan mode in a live cell imaging chamber at 37°C and 5% CO₂. HCT8-INAVA-GFP cells were plated at a density of 70%–80% confluence on the 35-mm μ -Dish (ibidi GmbH) 1 d before performing FRAP experiments. After the IL-1 β or H₂O₂ treatment, cells were scanned using a 63 \times oil immersion lens with the 488-nm laser intensity at 1–1.5. INAVA-GFP puncta with diameter of 1–1.5 μ m were fully photobleached with 100% laser power using a 488-nm laser with a bleach depth value at \sim 60% (bleaching scan speed at 6 s). Time-lapse images were acquired over a 3-min time course after bleaching using 2-s intervals. Images were processed by ImageJ, and FRAP data were fit to a single-exponential model using GraphPad Prism.

Data analysis was performed using previously published methods (Nissim-Rafinia and Meshorer, 2011). Fluorescence intensities of regions of interest (ROIs) in the bleaching area (ROIb), the background area (ROIbg), and the nonbleached nuclear area (ROIInb) were recorded for each time point. The final

data were normalized to prebleached intensities of the ROI data according to the equation $[(ROIb - ROIbg) / (ROIInb - ROIbg)] / [(pbROIb - pbROIbg) / (pbROIInb - pbROIbg)]$, where pb denotes prebleached.

Brightfield and epifluorescence imaging

A KEYENCE epifluorescent microscope was used to image HCT8 WT and HCT8-INAVA-GFP 3D epithelial cysts. For growth of 3D cysts, HCT8 WT and HCT8-INAVA-GFP were plated in Matrigel and treated with Y27632 (10 μ M) where indicated. Brightfield images were taken 1 wk later.

Images of doxycycline-inducible HCT8 myc-ARNO-(E156K) with or without stably expressed INAVA-GFP were also taken with the KEYENCE microscope. These cells were induced with doxycycline (1 μ g/ml) overnight. Cells were fixed with 4% PFA, permeabilized with 0.2% saponin, and blocked using 5% normal goat serum. Cells were stained with anti-myc (1:500) and labeled with secondary anti-mouse Alexa Fluor.

Confocal fluorescent imaging

A spinning disk confocal head (CSU-X1; PerkinElmer) coupled to an inverted Zeiss Axiovert 200M microscope (Carl Zeiss) were used for lateral membrane imaging of HCT8-INAVA-GFP and Caco2BBE-INAVA-GFP cells. HCT8-INAVA-GFP cells were plated overnight. The following day, cells were mocked or treated with ROCK inhibitors Y27632 (10 μ M), Y39983 (10 μ M), and myosin II inhibitor blebbistatin (50 μ M) for 1 h. Cells were fixed and processed as above and stained with anti-ZO-1 (1:500). The imaging system was operated using SlideBook (Intelligent Imaging Innovations).

A Zeiss 880 laser scanning confocal microscope with Fast Airyscan was used to image localization of doxycycline-inducible myc- β TrCP2 in HCT8 WT and HCT8-INAVA-GFP cells. The cells were induced with doxycycline (1 μ g/ml) overnight and treated with indicated condensate inducers. Cells were fixed at indicated time points and stained with anti-myc and secondary Alexa Fluor as described above.

Live cell imaging was performed with the Zeiss 880 laser scanning confocal microscope at 37°C in 5% CO₂. HCT8-INAVA-GFP cells were plated on the 35-mm μ -Dish (ibidi GmbH) 1 d before each live cell experiment. The following day, media were changed, and the cells were treated with IL-1 β (10 ng/ml) or H₂O₂ (1 mM) to induce condensate formation.

Colocalization with transferrin-positive endosomes and LAMP1 lysosomes was performed with IL-1 β -induced HCT8-INAVA-GFP cells. Cells were treated with transferrin-Alexa Fluor 647 (10 μ g/ml) and IL-1 β (10 ng/ml) for 30 min. Cells were washed, fixed with 4% PFA, and stained with α -LAMP1 (1:250) as a marker for lysosomes. Cells were imaged with a Zeiss 880 laser scanning confocal microscope.

Pulse-chase experiments were performed in HCT8-INAVA-GFP cells pulsed with MG132 (10 μ M), HSP90 (1 μ M), and H₂O₂ (1 mM) for 30 min. Cells were washed two times with PBS and replaced with fresh growth media. Cells were then placed back into the incubator and fixed with 4% PFA at indicated time points, stained, and imaged by high-content confocal microscopy as above.

HCT8-INAVA-GFP cells expressing doxycycline-inducible myc-ARNO (E156K) were treated with 1 $\mu\text{g}/\text{ml}$ doxycycline for 24 h. Cells were then treated with MG132 (10 μM), H_2O_2 (1 mM), and IL-1 β (10 ng/ml) for 90 min. Cells were fixed with 4% PFA and stained with anti-myc and imaged by laser scanning confocal microscopy or by ImageXpress Micro Confocal High Content Imaging System.

A Zeiss 880 laser scanning confocal microscope was used for live cell imaging of INAVA condensates. We calculated the movement of INAVA-GFP using TrackMate, an open-source Fiji plugin for the manual tracking of a single particle. The velocity for each puncta was calculated using the distance divided by the total recording time (360 s).

Western blot assays

Cell-based ubiquitination assays were performed in HEK293T WT cells transfected with HA-ubiquitin construct in stably expressed pLVXGFP-C1 empty vector, long and short GFP-INAVA, and GFP-INAVA C141A mutant. The next day, cells were replaced with fresh media and treated with H_2O_2 for 90 min. Cells were then washed twice with PBS and lysed in radioimmunoprecipitation assay buffer + 2 mM EDTA + protease inhibitors. Lysates were centrifuged at 20,000 g for 5 min and supernatants collected. The sample buffer was boiled and loaded onto SDS-PAGE gels and immunoblotted. Images were taken with the Azure c300 system. Western blot analysis of compound-treated cells were performed as indicated in the text and processed for SDS-PAGE and immunoblot analysis as above.

Luciferase assays

HCT8 WT and HCT8-INAVA-GFP cells were transiently transfected with NF- κB firefly luciferase and SV40-*Renilla reniformis* plasmid using Lipofectamine 2000 (Thermo Fisher Scientific). The following day, cells were pretreated with inhibitors for 30 min followed by treatment with IL-1 β (10 ng/ml) for 5 h. Luminescence was measured using the Tecan Spark 10M plate reader.

Statistical analysis

Mean values between two groups were compared using unpaired Student's t test (two sided). Data distribution was assumed to be normal, but this was not formally tested. In figures, significance is indicated as follows: *, $P < 0.05$; **, $P < 0.01$; ***, $P < 0.001$; ****, $P < 0.0001$. All analyses were performed in GraphPad Prism (GraphPad Software).

Online supplemental material

Fig. S1 provides additional description and validation of the screen for IL-1 β -induced INAVA condensates. **Fig. S2** and **Fig. S3** provide further characterization of INAVA puncta inducers and control experiments for βTrCP2 colocalization. **Fig. S4** shows all validated p38 and mTOR inhibitors discovered in the screen, characterization of H_2O_2 -induced INAVA puncta as biomolecular condensates, and schematic of the screen for puncta inhibitors. **Fig. S5** shows additional evidence that membrane and cytosolic localizations of INAVA are competing reactions. **Videos 1** and **2** show live cell imaging and fusion of IL-1 β -induced

INAVA condensates. **Video 3** shows FRAP of IL-1 β -induced INAVA condensates. **Video 4** shows live cell imaging of H_2O_2 -induced INAVA condensates. Table S1 shows the top 25 compounds that block H_2O_2 -induced INAVA condensates.

Acknowledgments

We thank Jennifer Smith, Jennifer Nale, David Wrobel, and the ICCB-Longwood for advice and guidance. **Fig. 8** was created with BioRender.com.

This work was supported by National Institutes of Health grant T32 DK747736 (D. Chang); the Crohn's and Colitis Foundation Career Development Award (P. Luong); National Institutes of Health grants DK122953 (W.I. Lencer and P. Luong) and DK048106 and DK084424 (W.I. Lencer); and Harvard Digestive Diseases Center grant P30 DK034854 (W.I. Lencer).

The authors declare no competing financial interests.

Author contributions: P. Luong and W.I. Lencer conceived of the project. D. Chang, P. Luong, and W.I. Lencer contributed to experimental design, data analysis and interpretation, and writing of the manuscript. P. Luong, Q. Li, J. LeBarron, and D. Chang executed the experiments. L. Barrett and M. Anderson contributed to imaging studies.

Submitted: 27 July 2020

Revised: 1 April 2021

Accepted: 26 May 2021

References

- Alberti, S. 2017. The wisdom of crowds: regulating cell function through condensed states of living matter. *J. Cell Sci.* 130:2789–2796. <https://doi.org/10.1242/jcs.200295>
- Alberti, S., and D. Dormann. 2019. Liquid-liquid phase separation in disease. *Annu. Rev. Genet.* 53:171–194. <https://doi.org/10.1146/annurev-genet-112618-043527>
- Alberti, S., and A.A. Hyman. 2021. Biomolecular condensates at the nexus of cellular stress, protein aggregation disease and ageing. *Nat. Rev. Mol. Cell Biol.* 22:196–213. <https://doi.org/10.1038/s41580-020-00326-6>
- Alberti, S., A. Gladfelter, and T. Mittag. 2019. Considerations and challenges in studying liquid-liquid phase separation and biomolecular condensates. *Cell.* 176:419–434. <https://doi.org/10.1016/j.cell.2018.12.035>
- Banani, S.F., A.M. Rice, W.B. Peeples, Y. Lin, S. Jain, R. Parker, and M.K. Rosen. 2016. Compositional control of phase-separated cellular bodies. *Cell.* 166:651–663. <https://doi.org/10.1016/j.cell.2016.06.010>
- Banani, S.F., H.O. Lee, A.A. Hyman, and M.K. Rosen. 2017. Biomolecular condensates: organizers of cellular biochemistry. *Nat. Rev. Mol. Cell Biol.* 18:285–298. <https://doi.org/10.1038/nrm.2017.7>
- Boeynaems, S., S. Alberti, N.L. Fawzi, T. Mittag, M. Polymenidou, F. Rousseau, J. Schymkowitz, J. Shorter, B. Wolozin, L. Van Den Bosch, et al. 2018. Protein phase separation: a new phase in cell biology. *Trends Cell Biol.* 28:420–435. <https://doi.org/10.1016/j.tcb.2018.02.004>
- Brangwynne, C.P., C.R. Eckmann, D.S. Courson, A. Rybarska, C. Hoegge, J. Gharakhani, F. Jülicher, and A.A. Hyman. 2009. Germline P granules are liquid droplets that localize by controlled dissolution/condensation. *Science.* 324:1729–1732. <https://doi.org/10.1126/science.1172046>
- Broom, O.J., B. Widjaya, J. Troelsen, J. Olsen, and O.H. Nielsen. 2009. Mitogen activated protein kinases: a role in inflammatory bowel disease? *Clin. Exp. Immunol.* 158:272–280. <https://doi.org/10.1111/j.1365-2249.2009.04033.x>
- Bureau, A., J.M. Beaulieu, T. Paccalet, Y.C. Chagnon, and M. Maziade. 2017. The interaction of GSK3B and FXR1 genotypes may influence the mania and depression dimensions in mood disorders. *J. Affect. Disord.* 213:172–177. <https://doi.org/10.1016/j.jad.2017.02.023>
- Coulthard, L.R., D.E. White, D.L. Jones, M.F. McDermott, and S.A. Burchill. 2009. p38(MAPK): stress responses from molecular mechanisms to

- therapeutics. *Trends Mol. Med.* 15:369–379. <https://doi.org/10.1016/j.molmed.2009.06.005>
- Danieli, A., and S. Martens. 2018. p62-mediated phase separation at the intersection of the ubiquitin-proteasome system and autophagy. *J. Cell Sci.* 131:jcs.214304. <https://doi.org/10.1242/jcs.214304>
- Dennis, M.D., L.S. Jefferson, and S.R. Kimball. 2012. Role of p70S6K1-mediated phosphorylation of eIF4B and PDCD4 proteins in the regulation of protein synthesis. *J. Biol. Chem.* 287:42890–42899. <https://doi.org/10.1074/jbc.M112.404822>
- Du, M., and Z.J. Chen. 2018. DNA-induced liquid phase condensation of cGAS activates innate immune signaling. *Science.* 361:704–709. <https://doi.org/10.1126/science.aat1022>
- Elbaum-Garfinkle, S. 2019. Matter over mind: liquid phase separation and neurodegeneration. *J. Biol. Chem.* 294:7160–7168. <https://doi.org/10.1074/jbc.REV118.001188>
- Fournier, M.J., C. Gareau, and R. Mazroui. 2010. The chemotherapeutic agent bortezomib induces the formation of stress granules. *Cancer Cell Int.* 10:12. <https://doi.org/10.1186/1475-2867-10-12>
- Fujimuro, M., H. Sawada, and H. Yokosawa. 1994. Production and characterization of monoclonal antibodies specific to multi-ubiquitin chains of polyubiquitinated proteins. *FEBS Lett.* 349:173–180. [https://doi.org/10.1016/0014-5793\(94\)00647-4](https://doi.org/10.1016/0014-5793(94)00647-4)
- Grothaus, J.S., G. Ares, C. Yuan, D.R. Wood, and C.J. Hunter. 2018. Rho kinase inhibition maintains intestinal and vascular barrier function by upregulation of occludin in experimental necrotizing enterocolitis. *Am. J. Physiol. Gastrointest. Liver Physiol.* 315:G514–G528. <https://doi.org/10.1152/ajpgi.00357.2017>
- Han, T.W., M. Kato, S. Xie, L.C. Wu, H. Mirzaei, J. Pei, M. Chen, Y. Xie, J. Allen, G. Xiao, and S.L. McKnight. 2012. Cell-free formation of RNA granules: bound RNAs identify features and components of cellular assemblies. *Cell.* 149:768–779. <https://doi.org/10.1016/j.cell.2012.04.016>
- Hofweber, M., S. Hutten, B. Bourgeois, E. Spreitzer, A. Niedner-Boblenz, M. Schifferer, M.D. Ruepp, M. Simons, D. Niessing, T. Madl, et al. 2018. Phase separation of FUS is suppressed by its nuclear import receptor and arginine methylation. *Cell.* 173:706–719.e13. <https://doi.org/10.1016/j.cell.2018.03.004>
- Ivanov, A.I., A.M. Hopkins, G.T. Brown, K. Gerner-Smidt, B.A. Babbin, C.A. Parkos, and A. Nusrat. 2008. Myosin II regulates the shape of three-dimensional intestinal epithelial cysts. *J. Cell Sci.* 121:1803–1814. <https://doi.org/10.1242/jcs.015842>
- Kato, M., Y.S. Yang, B.M. Sutter, Y. Wang, S.L. McKnight, and B.P. Tu. 2019. Redox state controls phase separation of the yeast ataxin-2 protein via reversible oxidation of its methionine-rich low-complexity domain. *Cell.* 177:711–721.e8. <https://doi.org/10.1016/j.cell.2019.02.044>
- Kopito, R.R. 2000. Aggresomes, inclusion bodies and protein aggregation. *Trends Cell Biol.* 10:524–530. [https://doi.org/10.1016/S0962-8924\(00\)01852-3](https://doi.org/10.1016/S0962-8924(00)01852-3)
- Leestemaker, Y., A. de Jong, K.F. Witting, R. Penning, K. Schuurman, B. Rodenko, E.A. Zaal, B. van de Kooij, S. Laufer, A.J.R. Heck, et al. 2017. Proteasome activation by small molecules. *Cell Chem. Biol.* 24:725–736.e7. <https://doi.org/10.1016/j.chembiol.2017.05.010>
- Lin, Y., D.S. Protter, M.K. Rosen, and R. Parker. 2015. Formation and maturation of phase-separated liquid droplets by RNA-binding proteins. *Mol. Cell.* 60:208–219. <https://doi.org/10.1016/j.molcel.2015.08.018>
- Luong, P., M. Hedl, J. Yan, T. Zuo, T.M. Fu, X. Jiang, J.R. Thiagarajah, S.H. Hansen, C.F. Lesser, H. Wu, et al. 2018. INAVA-ARNO complexes bridge mucosal barrier function with inflammatory signaling. *eLife.* 7:e38539. <https://doi.org/10.7554/eLife.38539>
- Lyon, A.S., W.B. Peebles, and M.K. Rosen. 2020. A framework for understanding the functions of biomolecular condensates across scales. *Nat. Rev. Mol. Cell Biol.* 22:215–235. <https://doi.org/10.1038/s41580-020-00303-z>
- Manzanillo, P., M. Mouchess, N. Ota, B. Dai, R. Ichikawa, A. Wuster, B. Haley, G. Alvarado, Y. Kwon, R. Caothien, et al. 2018. Inflammatory bowel disease susceptibility gene *CIORF106* regulates intestinal epithelial permeability. *Immunohorizons.* 2:164–171. <https://doi.org/10.4049/immunohorizons.1800027>
- Mateju, D., T.M. Franzmann, A. Patel, A. Kopach, E.E. Boczek, S. Maharana, H.O. Lee, S. Carra, A.A. Hyman, and S. Alberti. 2017. An aberrant phase transition of stress granules triggered by misfolded protein and prevented by chaperone function. *EMBO J.* 36:1669–1687. <https://doi.org/10.15252/embj.201695957>
- Mohanan, V., T. Nakata, A.N. Desch, C. Lévesque, A. Boroughs, G. Guzman, Z. Cao, E. Creasey, J. Yao, G. Boucher, et al. 2018. *Clorf106* is a colitis risk gene that regulates stability of epithelial adherens junctions. *Science.* 359:1161–1166. <https://doi.org/10.1126/science.aan0814>
- Mokas, S., J.R. Mills, C. Garreau, M.J. Fournier, F. Robert, P. Arya, R.J. Kaufman, J. Pelletier, and R. Mazroui. 2009. Uncoupling stress granule assembly and translation initiation inhibition. *Mol. Biol. Cell.* 20:2673–2683. <https://doi.org/10.1091/mbc.e08-10-1061>
- Nelms, B.D., L. Waldron, L.A. Barrera, A.W. Weflen, J.A. Goettel, G. Guo, R.K. Montgomery, M.R. Neutra, D.T. Breault, S.B. Snapper, et al. 2016. CellMapper: rapid and accurate inference of gene expression in difficult-to-isolate cell types. *Genome Biol.* 17:201. <https://doi.org/10.1186/s13059-016-1062-5>
- Nissim-Rafinia, M., and E. Meshorer. 2011. Photobleaching assays (FRAP & FLIP) to measure chromatin protein dynamics in living embryonic stem cells. *J. Vis. Exp.* (52):2696. <https://doi.org/10.3791/2696>
- Protter, D.S.W., and R. Parker. 2016. Principles and Properties of Stress Granules. *Trends Cell Biol.* 26:668–679. <https://doi.org/10.1016/j.tcb.2016.05.004>
- Riento, K., and A.J. Ridley. 2003. Rocks: multifunctional kinases in cell behaviour. *Nat. Rev. Mol. Cell Biol.* 4:446–456. <https://doi.org/10.1038/nrml128>
- Rivas, M.A., M. Beaudoin, A. Gardet, C. Stevens, Y. Sharma, C.K. Zhang, G. Boucher, S. Ripke, D. Ellinghaus, N. Burt, et al. International Inflammatory Bowel Disease Genetics Consortium. 2011. Deep resequencing of GWAS loci identifies independent rare variants associated with inflammatory bowel disease. *Nat. Genet.* 43:1066–1073. <https://doi.org/10.1038/ng.952>
- Sahai, E., and C.J. Marshall. 2002. ROCK and Dia have opposing effects on adherens junctions downstream of Rho. *Nat. Cell Biol.* 4:408–415. <https://doi.org/10.1038/ncb796>
- Saxton, R.A., and D.M. Sabatini. 2017. mTOR signaling in growth, metabolism, and disease. *Cell.* 168:960–976. <https://doi.org/10.1016/j.cell.2017.02.004>
- Sha, Y., L. Pandit, S. Zeng, and N.T. Eissa. 2009. A critical role for CHIP in the aggresome pathway. *Mol. Cell Biol.* 29:116–128. <https://doi.org/10.1128/MCB.00829-08>
- Shin, Y., and C.P. Brangwynne. 2017. Liquid phase condensation in cell physiology and disease. *Science.* 357:eaa4382. <https://doi.org/10.1126/science.aaf4382>
- Su, X., J.A. Ditlev, E. Hui, W. Xing, S. Banjade, J. Okrut, D.S. King, J. Taunton, M.K. Rosen, and R.D. Vale. 2016. Phase separation of signaling molecules promotes T cell receptor signal transduction. *Science.* 352:595–599. <https://doi.org/10.1126/science.aad9964>
- Sun, D., R. Wu, J. Zheng, P. Li, and L. Yu. 2018. Polyubiquitin chain-induced p62 phase separation drives autophagic cargo segregation. *Cell Res.* 28:405–415. <https://doi.org/10.1038/s41422-018-0017-7>
- Taipale, M., I. Krykbaeva, M. Koeva, C. Kayatekin, K.D. Westover, G.I. Karras, and S. Lindquist. 2012. Quantitative analysis of HSP90-client interactions reveals principles of substrate recognition. *Cell.* 150:987–1001. <https://doi.org/10.1016/j.cell.2012.06.047>
- Takata, A., N. Matsumoto, and T. Kato. 2017. Genome-wide identification of splicing QTLs in the human brain and their enrichment among schizophrenia-associated loci. *Nat. Commun.* 8:14519. <https://doi.org/10.1038/ncomms14519>
- Thomas, M.G., L.J. Martinez Tosar, M.A. Desbats, C.C. Leishman, and G.L. Boccaccio. 2009. Mammalian Staufen 1 is recruited to stress granules and impairs their assembly. *J. Cell Sci.* 122:563–573. <https://doi.org/10.1242/jcs.038208>
- Vermeulen, S.J., F. Nollet, E. Teugels, J. Philippe, F. Speleman, F.M. van Roy, M.E. Bracke, and M.M. Mareel. 1997. Mutation of alpha-catenin results in invasiveness of human HCT-8 colon cancer cells. *Ann. N. Y. Acad. Sci.* 833(1 Cancer):186–189. <https://doi.org/10.1111/j.1749-6632.1997.tb48607.x>
- Wang, Y., M. Begley, Q. Li, H.T. Huang, A. Lako, M.J. Eck, N.S. Gray, T.J. Mitchison, L.C. Cantley, and J.J. Zhao. 2016. Mitotic MELK-eIF4B signaling controls protein synthesis and tumor cell survival. *Proc. Natl. Acad. Sci. USA.* 113:9810–9815. <https://doi.org/10.1073/pnas.1606862113>
- Wheeler, R.J., H.O. Lee, I. Poser, A. Pal, T. Doeleman, S. Kishigami, S. Kour, E.N. Anderson, L. Marrone, A.C. Murthy, et al. 2019. Small molecules for modulating protein driven liquid-liquid phase separation in treating neurodegenerative disease. *bioRxiv:721001*. <https://doi.org/10.1101/721001>
- Xavier, R.J., and D.K. Podolsky. 2007. Unravelling the pathogenesis of inflammatory bowel disease. *Nature.* 448:427–434. <https://doi.org/10.1038/nature06005>
- Yan, J., M. Hedl, and C. Abraham. 2017. An inflammatory bowel disease-risk variant in INAVA decreases pattern recognition receptor-induced outcomes. *J. Clin. Invest.* 127:2192–2205. <https://doi.org/10.1172/JCI86282>
- Yasuda, S., H. Tsuchiya, A. Kaiho, Q. Guo, K. Ikeuchi, A. Endo, N. Arai, F. Ohtake, S. Murata, T. Inada, et al. 2020. Stress- and ubiquitylation-

- dependent phase separation of the proteasome. *Nature*. 578:296–300. <https://doi.org/10.1038/s41586-020-1982-9>
- Zhang, J.H., T.D. Chung, and K.R. Oldenburg. 1999. A simple statistical parameter for use in evaluation and validation of high throughput screening assays. *J. Biomol. Screen.* 4:67–73. <https://doi.org/10.1177/108705719900400206>
- Zhao, J., and A.L. Goldberg. 2016. Coordinate regulation of autophagy and the ubiquitin proteasome system by MTOR. *Autophagy*. 12:1967–1970. <https://doi.org/10.1080/15548627.2016.1205770>
- Zhao, J., B. Zhai, S.P. Gygi, and A.L. Goldberg. 2015. mTOR inhibition activates overall protein degradation by the ubiquitin proteasome system as well as by autophagy. *Proc. Natl. Acad. Sci. USA*. 112:15790–15797. <https://doi.org/10.1073/pnas.1521919112>
- Zou, Y., L. Ma, Y. Zhao, S. Zhang, C. Zhou, and Y. Cai. 2018. Inhibition of Rho kinase protects against colitis in mice by attenuating intestinal epithelial barrier dysfunction via MLC and the NF- κ B pathway. *Int. J. Mol. Med.* 41:430–438.

Supplemental material

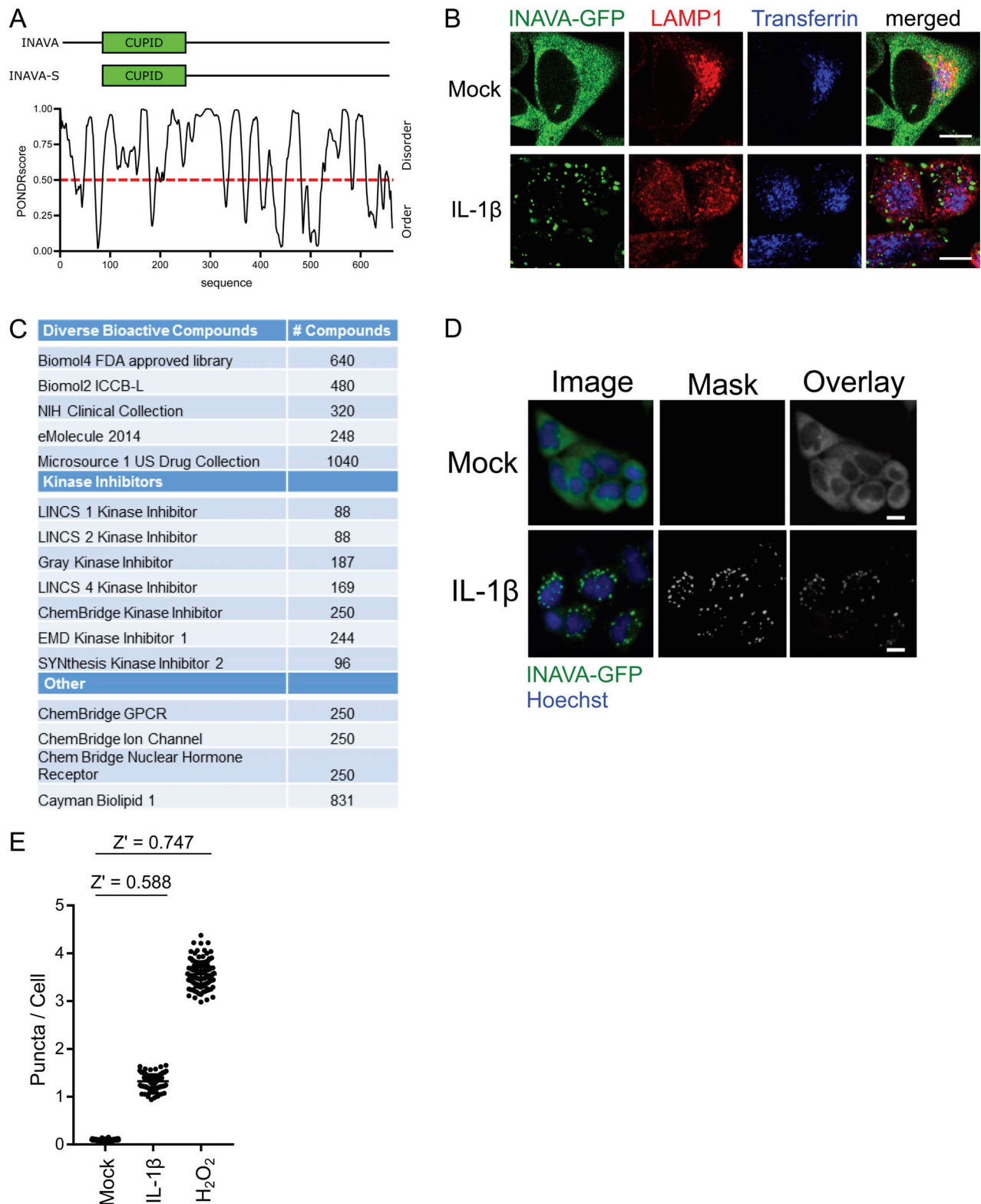


Figure S1. **Description and validation of the screen for IL-1 β -induced INAVA condensates.** (A) Predictor of Natural Disordered Regions (PONDR) score displaying intrinsic disordered and ordered regions of the long and short isoforms of INAVA. (B) INAVA does not colocalize with lysosomes or endosomes. IL-1 β -induced HCT8-INAVA-GFP cells were treated with transferrin-Alexa Fluor 647 (10 μ g/ml) for 30 min as a marker for endosomes. Cells were washed, fixed with 4% PFA, and stained with α -LAMP1 as a marker for lysosomes. Images were taken using confocal microscopy. Scale bar = 10 μ m. (C) Table of small compound libraries screened in our study. (D) Representative image of the automated analysis used for INAVA-GFP puncta quantification. Hoechst (nuclei). Scale bar = 10 μ m. (E) Automated Z-factor for IL-1 β - and H₂O₂-induced INAVA-GFP puncta screens. EMD, EMD Biosciences; FDA, US Food and Drug Administration; GPCR, G-Protein Coupled Receptor; L, Longwood; LINCS, Library of Integrated Network-Based Cellular Signatures; NIH, National Institutes of Health.

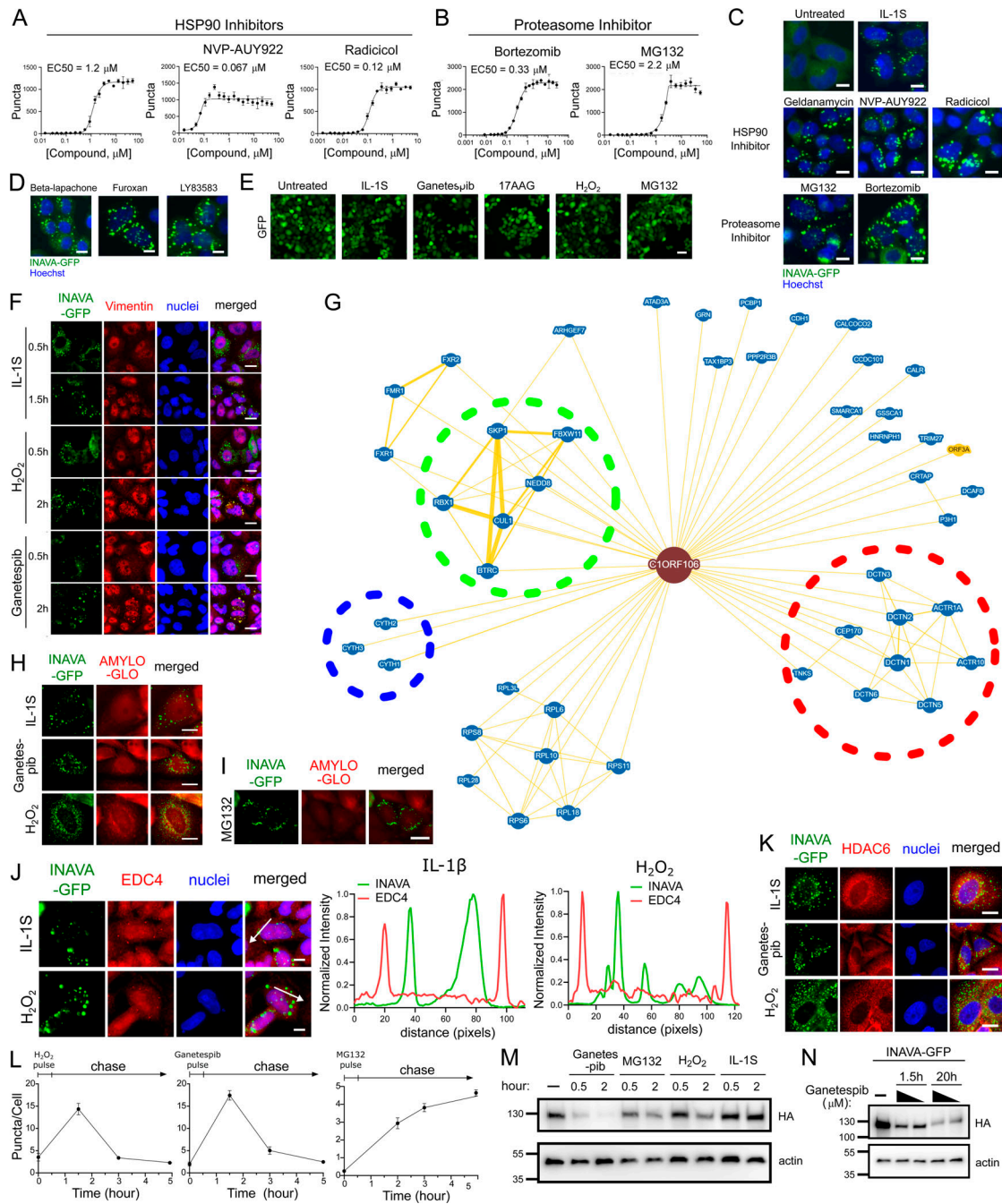


Figure S2. Characterization of INAVA puncta inducers. (A and B) Dose–response curves of (A) HSP90 inhibitors or (B) proteasome inhibitors. Images were taken by high-content imaging at 20× magnification with four positions/well, mean ± SEM, *n* = 3. **(C)** Representative images from A and B. Scale bar = 10 μm. **(D)** Representative images from ROS inducers identified in the INAVA puncta inducer screen. Scale bar = 10 μm. **(E)** HCT8 cells stably expressing only GFP were treated with corresponding compounds for 90 min, fixed, and imaged. Scale bar = 40 μm. **(F)** HCT8-INAVA-GFP cells treated with IL-1β (10 ng/ml), H₂O₂ (1 mM), or ganetespiib (1 μM) for the early and late time points indicated. Cells were fixed and stained with vimentin. Scale bar = 20 μm. **(G)** INAVA protein–protein interactors annotated in BioGRID (<https://thebiogrid.org>). Dashed circles highlight interactors, including cytoskeleton family members (blue) and multisubunit ubiquitin E3 complexes (green). The multisubunit dynein complex (red) involved in the aggresome pathway was also identified. **(H and I)** HCT8-INAVA-GFP cells were treated with (H) IL-1β (10 ng/ml), ganetespiib (1 μM), MG132 (10 μM), or (I) H₂O₂ (1 mM) for 90 min. Cells were fixed and stained with AMYLO-GLO. Scale bar = 20 μm. **(J)** HCT8-INAVA-GFP cells were treated with IL-1β (10 ng/ml) or H₂O₂ (1 mM) for 90 min and stained with EDC4 (left panel). Fluorescent line scans (arrow) of INAVA (green) and EDC4 (red) are displayed (right panel). Scale bar = 10 μm. **(K)** HCT8-INAVA-GFP cells were treated with IL-1β (10 ng/ml), ganetespiib (1 μM), or H₂O₂ (1 mM) for 90 min and stained with HDAC6. Scale bar = 20 μm. **(L)** Pulse-chase experiments in HCT8 INAVA-GFP cells treated with IL-1β (10 ng/ml), H₂O₂ (1 mM), or ganetespiib (1 μM) for 30 min. Following treatment, cells were washed with complete media, chased, and analyzed at the time points indicated, mean ± SEM, *n* = 2. **(M)** HCT8-INAVA-GFP cells were treated with condensate inducers as above, including MG132 (10 μM) at the indicated time points. Cells were harvested and analyzed for Western blotting. Anti-HA measures HA tag present in INAVA-GFP, and actin was used as a loading control. **(N)** Same as D but treated with ganetespiib (1 μM and 300 nM). Samples were collected at 1.5 h and 20 h for Western blot analysis. The unit of measure for the Western blots is kilodaltons.

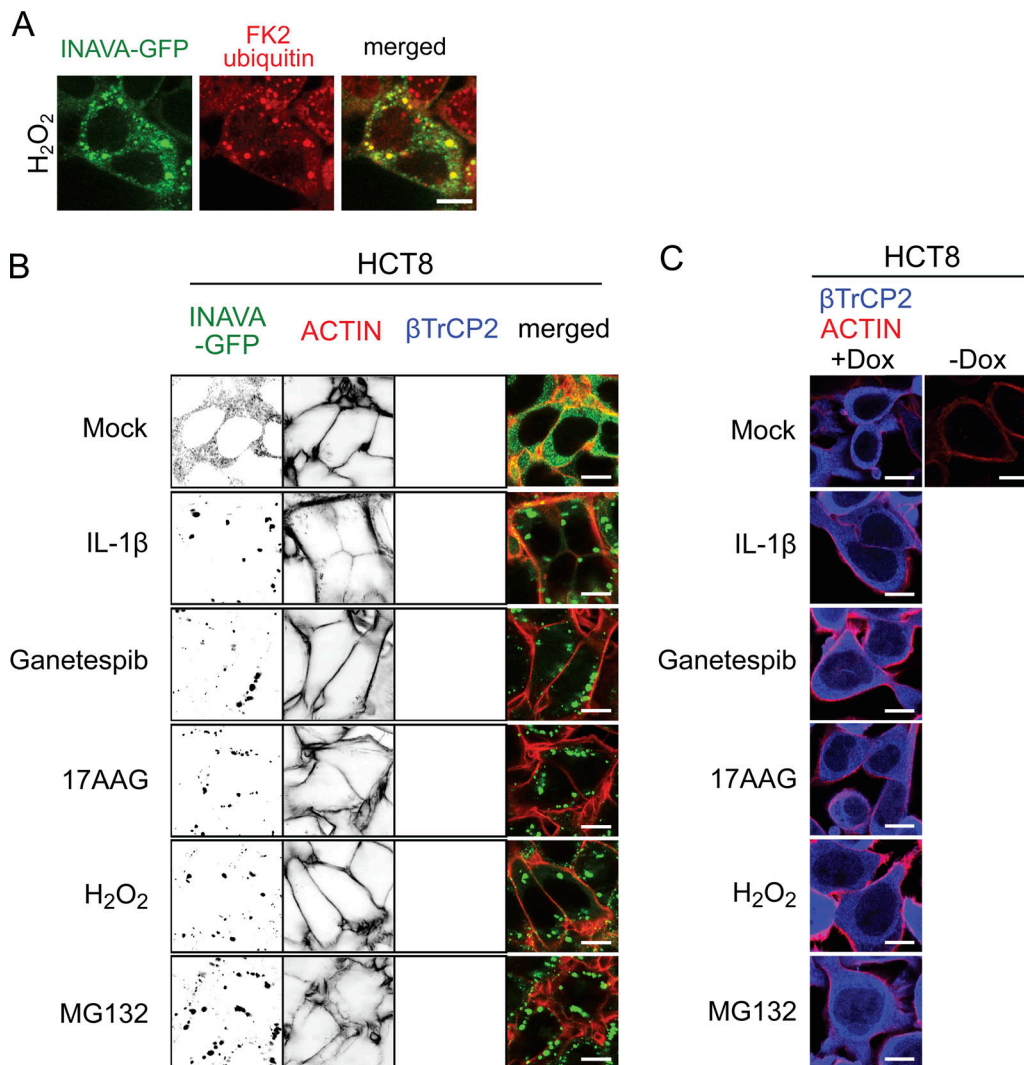


Figure S3. **H₂O₂-induced INAVA condensates colocalize with conjugated ubiquitin: control experiments for β TrCP2 colocalization.** (A) HCT8-INA-A-GFP cells were treated with H₂O₂ (1 mM) for 90 min and stained with conjugated ubiquitin antibody FK2. Scale bar = 10 μ m. (B) Control images for Fig. 4 B of cells expressing only INAVA-GFP. HCT8-INA-A-GFP cells expressing doxycycline (Dox)-inducible myc- β TrCP2 without Dox treatment. Cells treated with condensate inducers as in Fig. 4 B. Cells were fixed and stained with phalloidin-TRITC (F-actin) and α -myc. (C) HCT8 cells stably expressing Dox-inducible myc- β TrCP2. Cells were treated overnight with Dox (1 μ g/ml), fixed, and stained with phalloidin-TRITC and α -myc. Scale bar = 10 μ m.

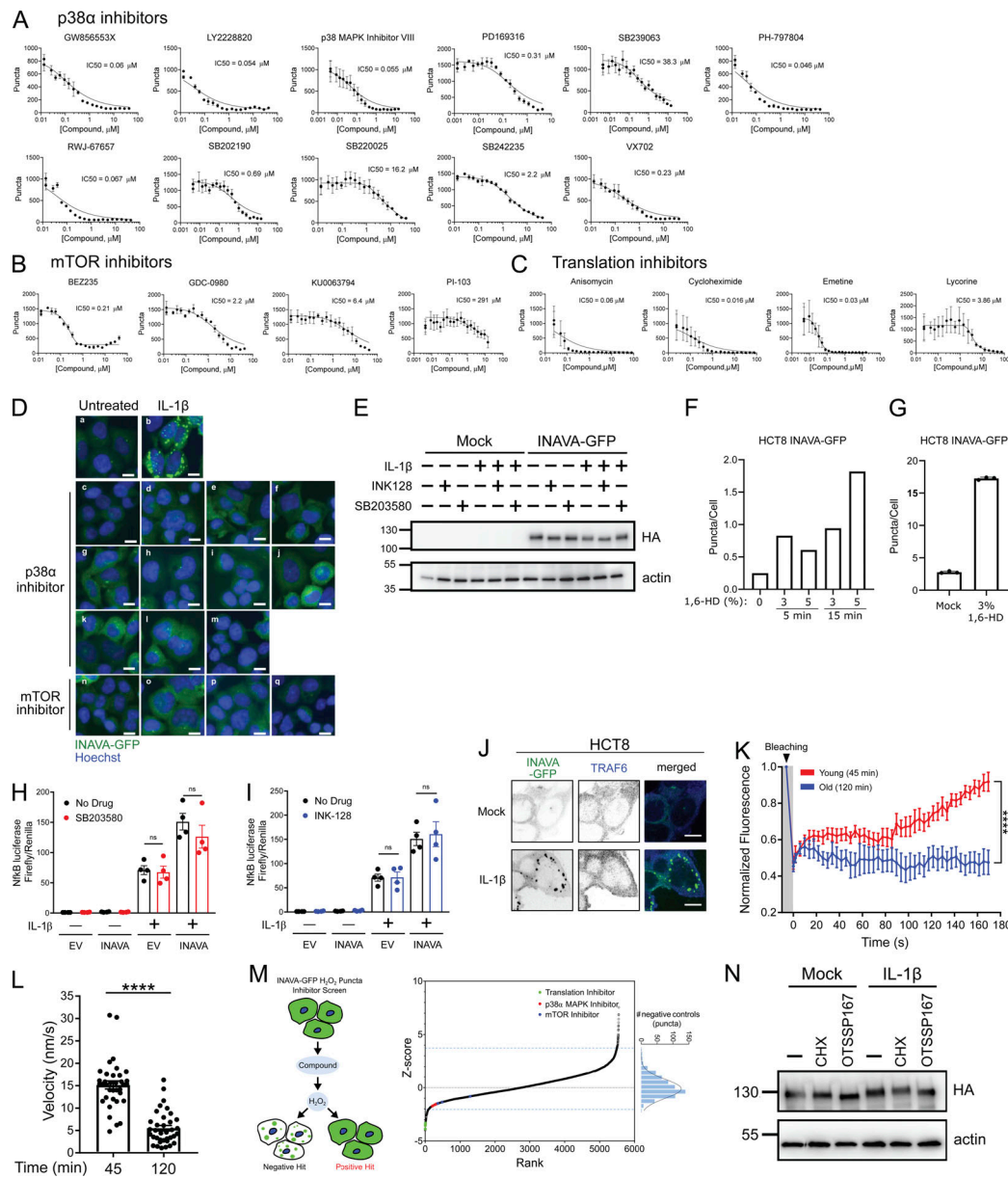


Figure S4. **Validated p38α and mTOR inhibitors discovered in the screen, characterization of H₂O₂-induced INAVA puncta as biomolecular condensates, and schematic of the screen for puncta inhibitors.** (A–C) Dose–response curves of all (A) p38α inhibitors, (B) mTOR inhibitors, and (C) translation inhibitors validated from the IL-1β–induced INAVA puncta inhibition screen. Images were taken by high-content imaging at 20× magnification at four positions/well, mean ± SEM, n = 3. (D) Representative images from dose–response experiments (p38α inhibitors [c–m]: p38α inhibitor VIII, PD169316, RWJ-67657, LY2228820, VX702, SB202190, SB239063, PH-797804, GW856553X, SB242235, SB220025; mTOR inhibitors [n–q]: GDC-0980, BEZ235, KU0063794, PI-103). Hoechst (nuclei). Scale bar = 10 μm. (E) HCT8-INAVA-GFP cells were pretreated with INK128 (10 μM) or SB203580 (10 μM) for 30 min followed by treatment with IL-1β for 90 min. Cells were harvested and analyzed by Western blotting. Anti-HA detects INAVA-GFP, and actin was used as loading control. (F) HCT8-INAVA-GFP cells were treated with 3% and 5% 1,6-hexanediol (HD) for 5 and 15 min and were analyzed for INAVA-GFP puncta, mean ± SD. (G) Same as F but the time point at 30 min with 3% 1,6-HD, n = 3. (H and I) NF-κB luciferase reporter assay with (H) p38α inhibitor SB203580 or (I) mTOR inhibitor INK128. HEK293T cells transfected with empty vector (EV) or INAVA, NF-κB firefly luciferase and SV40-R. reniformis were pretreated with SB203580 or INK128 for 1 h and then treated with IL-1β (10 ng/ml) for 4 h and assayed for luminescence. Each point represents average luminescence for all replicates within each experiment, N = 49 per condition, four independent experiments performed, mean ± SD. (J) HCT8-INAVA-GFP cells expressing doxycycline-inducible myc-TRAF6. Cells were treated overnight with doxycycline (1 μg/ml) and then treated with IL-1β (10 ng/ml) for 60 min. Cells were fixed, stained with α-myc to detect myc-TRAF6 and processed by spinning disk confocal imaging. Scale bar = 10 μm. (K) FRAP of H₂O₂-induced INAVA-GFP “young” (45 min; n = 6) and “old” (120 min; n = 5) puncta in HCT8-INAVA-GFP cells. Bleaching was performed at the indicated time point (arrow), and recovery was allowed to occur at 37°C in 5% CO₂, mean ± SEM. (L) Velocity tracking of H₂O₂-induced INAVA-GFP puncta formed at different time points, mean ± SEM, n = 36. (M) Schematic of screen to identify inhibitors of H₂O₂-induced INAVA-GFP puncta (left panel) in HCT8 cells. Shown are ranked Z-scores of hits (right panel) and relative ranking of select compounds of interest: inhibitors of protein translation (green), MAPK p38α (red), or mTOR (blue). Frequencies of distribution of negative controls are displayed to the right of the graph. (N) HCT8-INAVA-GFP cells were pretreated with cycloheximide (CHX; 10 μM) or MELK inhibitor OTSSP167 (10 μM) for 30 min followed by IL-1β (10 ng/ml) for 1 h. Cells were harvested and analyzed for Western blotting. Anti-HA measures HA tag present in INAVA-GFP, and actin was used as a loading control. ****, P < 0.0001. The unit of measure for the Western blots is kilodaltons.

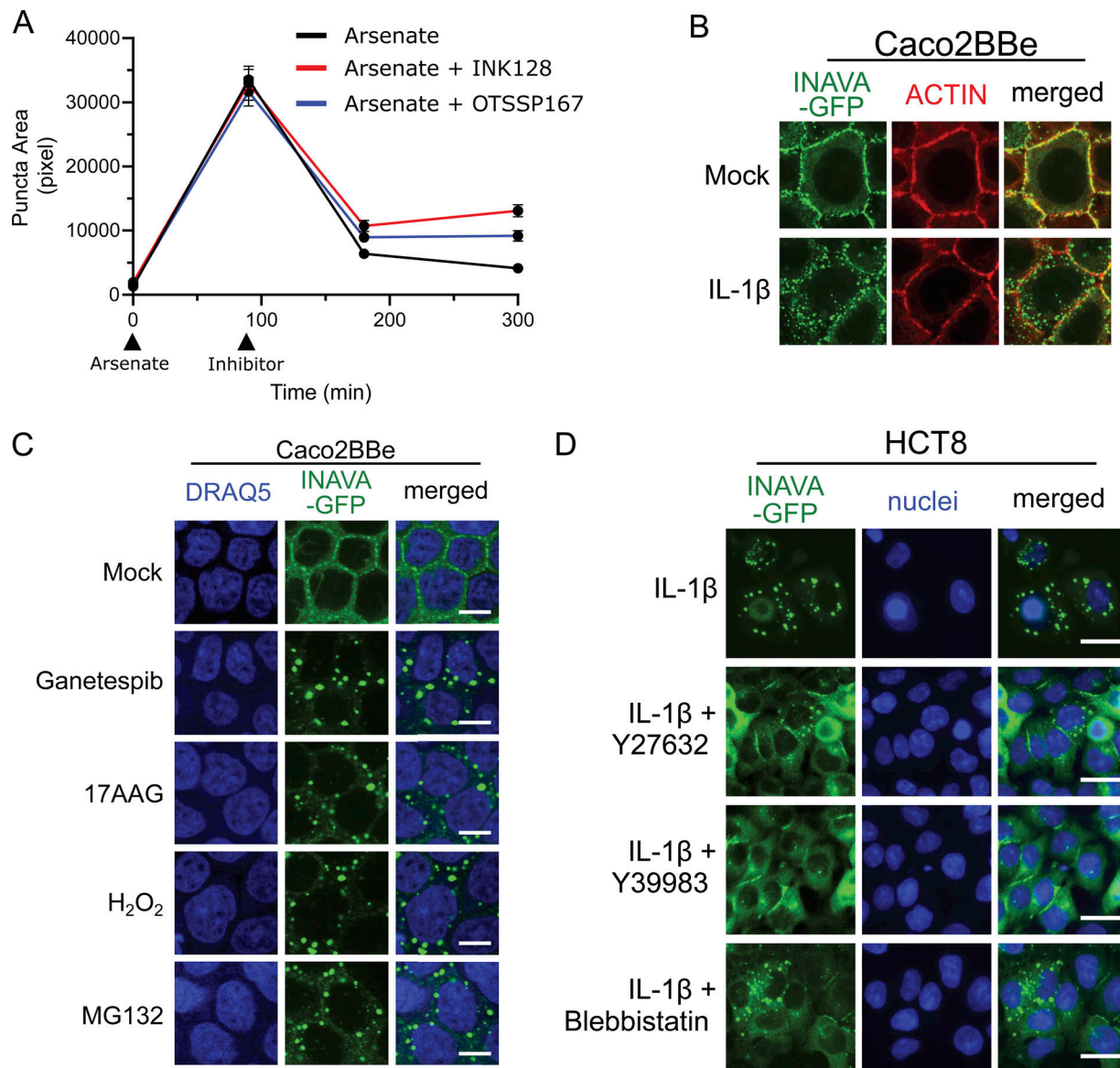


Figure S5. **INK128 and OTSSP167 block FUS-GFP puncta; membrane and cytosolic localizations of INAVA are competing reactions.** (A) HeLa FUS-GFP cells were treated with sodium arsenate (1 mM) for 90 min to allow FUS-GFP puncta formation. Cells were then treated with INK128 (10 μM) or OTSSP167 (10 μM). Cells were fixed at indicated time points and analyzed, mean ± SEM, n = 5. (B) INAVA-GFP localize to the membrane in Caco2BBE cells stably expressing INAVA-GFP (Caco2BBE-INAVA-GFP). Cells treated with IL-1β (10 ng/ml) for 1 h form INAVA-GFP puncta. Phalloidin-TRITC (actin). (C) Caco2BBE-INAVA-GFP cells were treated with ganetespiB (1 μM), 17AAG (10 μM), or H₂O₂ (1 mM) for 90 min and MG132 (10 μM) for 2 h. Fixed cells were stained with DRAQ5 (nuclei). Scale bar = 10 μm. (D) HCT8-INAVA-GFP cells were pretreated with Y27632, Y3998, and blebbistatin (33 μM for each compound) for 180 min. Cells were then treated with IL-1β (10 ng/ml) for 90 min, fixed, and imaged. Hoechst (nuclei). Scale bar = 20 μm.

Video 1. **Live cell imaging of HCT8-INAVA-GFP cells treated with IL-1β (10 ng/ml).** Images taken 0–60 min following treatment. 30 s/frame.

Video 2. **Live cell imaging of IL-1β-induced INAVA condensate fusion in HCT8-INAVA-GFP cells.** 1 s/frame.

Video 3. **FRAP experiment of HCT8-INAVA-GFP cells treated with IL-1 β (10 ng/ml).** 2 s/frame.

Video 4. **Live cell imaging of HCT8-INAVA-GFP cells treated with H₂O₂ (1 mM).** Images taken 15–75 min following treatment. 30 s/frame.

Provided online is one table. Table S1 shows the top 25 compounds that block H₂O₂-induced INAVA condensates.